RESEARCH ARTICLE

Winter-to-summer transition of Arctic sea ice breakup and floe size distribution in the Beaufort Sea

Byongjun Hwang[*], Jeremy Wilkinson[†], Ted Maksym[‡], Hans C. Graber[§], Axel Schweiger[||], Christopher Horvat[¶], Donald K. Perovich[**,††], Alexandra E. Arntsen[**], Timothy P. Stanton[‡‡], Jinchang Ren[§§] and Peter Wadhams[||||]

Breakup of the near-continuous winter sea ice into discrete summer ice floes is an important transition that dictates the evolution and fate of the marginal ice zone (MIZ) of the Arctic Ocean. During the winter of 2014, more than 50 autonomous drifting buoys were deployed in four separate clusters on the sea ice in the Beaufort Sea, as part of the Office of Naval Research MIZ program. These systems measured the ocean-ice-atmosphere properties at their location whilst the sea ice parameters in the surrounding area of these buoy clusters were continuously monitored by satellite TerraSAR-X Synthetic Aperture Radar. This approach provided a unique Lagrangian view of the winter-to-summer transition of sea ice breakup and floe size distribution at each cluster between March and August. The results show the critical timings of a) temporary breakup of winter sea ice coinciding with strong wind events and b) spring breakup (during surface melt, melt ponding and drainage) leading to distinctive summer ice floes. Importantly our results suggest that summer sea ice floe distribution is potentially affected by the state of winter sea ice, including the composition and fracturing (caused by deformation events) of winter sea ice, and that substantial mid-summer breakup of sea ice floes is likely linked to the timing of thermodynamic melt of sea ice in the area. As the rate of deformation and thermodynamic melt of sea ice has been increasing in the MIZ in the Beaufort Sea, our results suggest that these elevated factors would promote faster and more enhanced breakup of sea ice, leading to a higher melt rate of sea ice and thus a more rapid advance of the summer MIZ.

1. Introduction
Sea ice breakup is an important process that characterizes the winter-summer transition of sea ice in the marginal ice zone (MIZ). During winter, Arctic sea ice forms a continuous heterogeneous sheet that consists of ice of different ages and thickness, from multiyear ice (MYI, second-year ice or older) to newly formed ice within leads. As this winter ice drifts, the internal pressure field occasionally increases to such an extent that the ice fractures, producing localized deformation events and forming ridges or leads/cracks (Hwang et al., 2015).

In late spring and summer, the ice finally breaks apart into distinctive segments of sea ice called "floes". Large floes break into smaller floes either by floe-floe interactions, through a flexural failure by ocean surface waves (Langhorne et al., 1998; Dumnont et al., 2011; Williams et al., 2013a, 2013b, 2017), or/and through deforming failure induced by wind or current especially for thermodynamically weakened sea ice (Perovich et al., 2001; Arntsen et al., 2015). The production of smaller floes is important, as a group of smaller floes is more susceptible to lateral melting than a larger floe (Steele,

[*] Scottish Association for Marine Science, Oban, Argyll, PA37 1QA, UK

[†] British Antarctic Survey, Cambridge, UK

[‡] Woods Hole Oceanographic Institution, Woods Hole MA, US

[§] Rosenstiel School of Marine and Atmospheric Science, University of Miami, Miami, Florida, US

[||] Polar Science Center, Applied Physics Laboratory, University of Washington, Seattle, US

[¶] Harvard University, Cambridge, MA, US

[**] Thayer School of Engineering, Dartmouth College, Hanover, New Hampshire, US

[††] ERDC-CRREL, Hanover, New Hampshire, US

[‡‡] Naval Postgraduate School, Monterey CA, US

[§§] University of Strathclyde, Glasgow, UK

[||||] Unversity of Cambridge, Cambridge, UK

Corresponding author: Byongjun Hwang (phil.hwang@sams.ac.uk)

1992). This effect in turn allows increased radiative warming in the upper ocean, thus accelerating the melting of the floes (Perovich et al., 2008). This positive feedback influences the evolution of the sea ice in the summer MIZ.

The size distribution of sea ice floes, commonly known as floe size distribution (FSD), characterizes the sub-grid-scale composition of the sea ice field. The FSD is a probability distribution $f(x)$, where $f(x)dx$ is the fraction of a domain composed of ice with a floe size x, a measure of the lateral extent of the floes, between x and $x + dx$. Observations are typically reported in terms of the floe number distribution (FND), $n(x)$, where $n(x) \sim f(x)/\pi x^2$. In previous studies, the FND is defined as a power-law distribution, $n(x) = cx^{-\alpha}$, where x is the size of a sea ice floe, c is a constant, and α is the power-law exponent (Rothrock and Thorndike, 1984). If logarithms are taken on both $n(x)$ and x, i.e., $\log(n) = \log(c) - \alpha\log(x)$, the slope of the straight line on the log-log plot is $-\alpha$. The power-law distribution is also expressed as the (complementary) cumulative floe size number distribution (CFND), i.e., $N(x) = \Pr(X > x) \sim L(x)x^{-\alpha + 1}$, where $\alpha > 1$ and $L(x)$ is a slowly varying function (Rothrock and Thorndike, 1984; Bingham et al., 1989). In this case, the straight line on the log-log plot of $N(x)$ and x is $-\alpha+1$. Finding α (whether on FND or on CFND) requires a subjective assessment for the range over which a linear fit provides an appropriate model and a proper choice of binning method (Stern et al., 2017a). The derived exponent α, then, summarizes the state of FSD. For a higher α, there are relatively more small floes than large floes, and therefore a transition from lower α to higher α implies the breakup of larger floes into smaller floes. Identification of these transition points is important to understand the underlying physical processes that control the breakup of the ice pack.

The exponent α has been commonly estimated by fitting a straight line on a log-log plot (for either FND or CFND) using least-square fit (LSF) (e.g., Rothrock and Thorndike, 1984; Toyota et al., 2011 and 2006; Wang et al., 2016; Stern et al., 2017a and 2017b). A recent study by Clauset et al. (2009) and Virkar and Clauset (2014) suggested a method to calculate the exponent α for any given dataset by using the maximum likelihood estimator. In the LSF based method, one relies on a subjective judgment of where the straight line lies and how valid it is as a power-law distribution. In contrast, the method suggested by Virkar and Clauset (2014) provides a statistically sound estimate for the exponent α, the lower bound to the power-law behavior x_{min}, and a goodness-of-fit to test (p-value) of whether the data in question represent a power-law distribution or not (see Appendix B).

It is important to note that the Virkar and Clauset (2014) method (VC14) is an effective statistical estimate of a power-law fit to the FND tail. It should not be seen as verifying whether the FND is scale-invariant. The procedure identifies the most appropriate range of sizes above which the tail of the FND is plausibly fit by a power law. Often this range covers less than one tenth of observed floe sizes, and excludes a significant number of small floes and consequently a large percentage of the total ice area may be missing. The question of how to understand the FSD evolution and the potential emergence of power-law scaling features in the tail is an area of active research (Stern et al., 2017a; Chris Horvat, personal communication).

Sea ice floe size x has been previously defined as the mean caliper diameter (hereafter d) of the floe (e.g., Rothrock and Thorndike, 1984), or the diameter of the disc (e.g., Toyota et al., 2006 and 2011) or a side of the square (e.g., Steer et al., 2008) that has the equivalent floe area. The choice of x depends on the geometry (or shape) of the floes that can be inferred from floe properties (i.e., area, perimeter, mean, minimum and maximum caliper diameters). The ratios of those floe properties, reported in previous studies, show some variability compared with the values from a disc or a square (Rothrock and Thorndike, 1984; Hudson, 1987; Toyota and Enomoto, 2002; Toyota et al., 2006) (see Appendix C for more details on floe properties). If the floe shapes are irregular, the mean caliper diameter d provides the most realistic representation of the floe size.

Previous studies on sea-ice breakup and FSD transition have been conducted over a relatively short period of time and focused on particular events. For example, the study by Holt and Martin (2001) concentrated on a storm event during August 14–20, 1992, using ERS-1 SAR data. Toyota et al. (2006) examined the effects of lateral melt of small floes, based on a ship-born video and Landsat/ETM+ data collected for a day in February 2003 in the Sea of Okhotsk. The study by Wang et al. (2015) examined the transition of FSD during large wave events in August and September in the Beaufort Sea, focusing on the effects of ocean waves on floe breakup in a late summer condition. So far, no study has been conducted to examine a full winter-to-summer transition of sea ice breakup and FSD.

During the U.S. Office of Naval Research (ONR) MIZ program, four separate clusters (separated by about 100 km) of autonomous multi-sensor buoy systems, that measure a wide range of ocean, atmosphere and sea ice parameters, were deployed (Lee et al., 2012). During the experiment, GPS locations of each buoy in a cluster were tracked in near-real time, guiding acquisition of high-resolution (pixel spacing = 1.23 m) TerraSAR-X (TS-X) Synthetic Aperture Radar (SAR) data at the drifting cluster location. This comprehensive collection of TS-X SAR data was made at high temporal coverage (~2–5 days at each cluster) (see Table S1). This approach provides a unique view of a full winter-to-summer transition of sea ice breakup and FSD at the drifting clusters. The acquired TS-X SAR data were analyzed to derive open water fraction, MYI fraction and size, and summer sea ice FSD by using the algorithm described in Hwang et al. (2017). The purpose of this study is to provide a comprehensive overview of the winter-to-summer transition of sea ice breakup and FSD, by analyzing the TS-X derived parameters and their relationships to oceanic, atmospheric and sea ice parameters measured by clusters of multi-sensor buoys.

2. Dataset and methods
2.1 ONR MIZ buoy clusters and other datasets
During the 2014 ONR MIZ field campaign, clusters of multi-sensor buoys were deployed in late March 2014 between 72.5°N and 75.4°N along 135°W (see star symbols in **Figure 1a**). The buoys deployed in the clusters include the Ice-Tethered Profiler with Velocity (ITP-V), Ice Mass Balance Buoy (IMB), Automatic Weather Station (AWS), Wave Buoy (WB) and Arctic Ocean Flux Buoy (AOFB) (Lee et al., 2012). Cluster #1 (C1), the southernmost cluster, consisted of one AWS, five IMBs and five WBs. One of each buoy type was deployed at the center, and the remaining four IMBs and WBs were deployed at the corners of a 5-km grid around the center, known as a 5-dice array. At Clusters #2–#4 (C2–4), the buoy configuration was the same, but an ITP-V and AOFB were included at the center location. At C2, an additional IMB (2014C) from the Cold Regions Research and Engineering Laboratory (CRREL)

(Polashenski et al., 2011) was deployed at the center of the cluster, along with the ITP-V and AOFB.

ERA Interim 10-m wind data (European Centre for Medium-Range Weather Forecasts, 2014) (6 hourly, Reduced N256 Gaussian gridded surface level analysis time parameter data, ggas) was obtained from the British Atmospheric Data Centre (BADC). The wind data were extracted for the nearest data grid to the location of the reference buoy at each cluster. Wind speeds from ERA Interim are consistent with, but higher than wind speeds from AWS (2-m wind, uncorrected for ice motion). Advanced Microwave Scanning Radiometer-2 (AMSR-2) sea ice concentration (SIC) data (Spreen et al., 2008) were obtained from the sea ice data archive at the University of Bremen (www.seaice.uni-bremen.de). Open water fraction was calculated from SIC data for the data points that were extracted within the 15-km radius from the location of the reference buoy at each cluster.
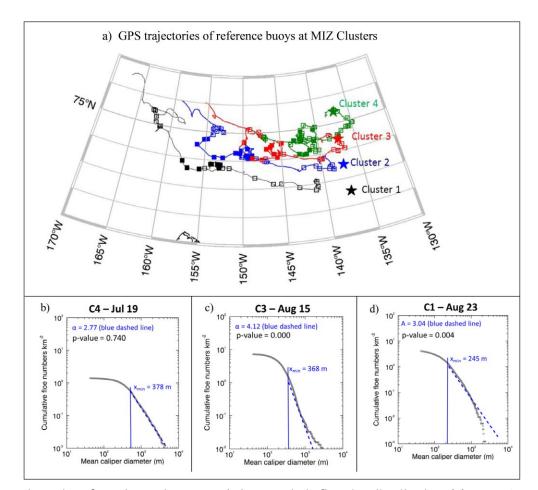

Figure 1: Trajectories of MIZ buoy clusters and characteristic floe size distribution. (a) GPS trajectories of the reference buoys for MIZ buoy clusters between May 1 and September 30, 2014. Trajectories are shown in solid lines for a selected reference buoy that was initially located at the centre of the buoy cluster. Empty square symbols mark the location of TS-X images used for the retrieval of open water fraction, and filled square symbols mark the location of TS-X images analyzed for floe size distribution (FSD) in this study. Star symbols mark the location of the buoys on March 20, 2014. The reference buoy for each cluster is IMB13 (Cluster 1), ITP-V 77 (Cluster 2), ITP-V 78 (Cluster 3), and ITP-V 79 (Cluster 4). Plots in panels **(b)–(d)** show FSD results in a log-log plot of cumulative floe number density for selected dates. Panel (b) provides a typical example of FSD results in July in which the goodness-of-the-fit test passed (p-value ≥ 0.1); (c) and (d) show the cases in which the goodness-of-fit test failed (p-value < 0.1). In plots in panels (b)–(d), α x_{min}, and p-value were calculated following Virkar and Clauset (2014). DOI: https://doi.org/10.1525/elementa.232.f1

Multisensor analyzed sea ice extent for the northern hemisphere (MASIE-NH) data were downloaded from the National Ice Center (NIC) and National Snow and Ice Data Center (NSIDC) (NSIDC, 2017). MASIE-NH data were compiled daily in various formats. The image data in GeoTiff format, containing flag for five different surface types at the 4-km pixel size, were used for this study. The nearest open water pixel was identified for each cluster, and then the distance between the cluster and the corresponding open water pixel was calculated. Small openings of open water within sea ice area can cause erroneous detection of the nearest ice edge. To avoid such errors, the nearest open water pixel that was connected to a large body of open water (at least 100 pixels or at least 1,600 km^2) was selected.

2.2 Satellite data

The acquisition of satellite data was near continuous in order to follow the evolution of ice conditions in the area of the MIZ buoy clusters. The acquired satellite data include TerraSAR-X (TS-X) Synthetic Aperture Radar (SAR), and high-resolution visible-band image (HRVI), also referred to as literal imagery derived products (LIDPs) (Duke, 2012), archived in Global Fiducials Library (GFL) (http://gfl.usgs.gov/) at the U.S. Geological Survey (USGS). TS-X SAR consisted of a large number of StripMap (SM) single-polarization (HH) data (pixel spacing = 1.25 m, swath size = ~30 × 60 km), and a small number of ScanSAR (SC) single-polarization (HH) data (pixel spacing = 8.25 m, swath size = ~100 × 100 km) data. The TS-X SAR SM data were acquired by the Center for Southeastern Tropical Advanced Remote Sensing (CSTARS) at the University of Miami as a part of the MIZ program, through careful planning of acquisition at a predicted location of a target buoy for each cluster. Additional TS-X SC SAR data were acquired at each cluster, through a TS-X science project with the German Aerospace Center (DLR). GFL HRVI (pixel spacing = 1 m) data were acquired through the declassification effort by the MEDEA group (Kwok and Untersteiner, 2011). In this study, TS-X SAR was used to derive open water fraction, ice type, and FSD (see **Figure 1a**).

2.3 Satellite data processing

For the retrieval of open water fraction, sea ice type and FSD, the algorithm described in Hwang et al. (2017) was used. The algorithm is composed of various image analysis methods, including Kernel Graph Cuts (KGC) to segment SAR imagery into water-ice regions, the distance transformation and watershed transform to split touching ice floes, as well as a rule-based post-processing for the revalidation of segmentation boundaries. Prior to the algorithm application, the whole swath of TS-X SM images was made into a sub-image of about 30 × 30 km centered on the reference buoy for each cluster. The resolution of the sub-images was then degraded by 75% (equivalent pixel spacing = 8.33 m), in order to process a large volume of SAR data.

At the reduced resolution, the derived FSD results significantly underestimated the number of small floes (less than 200 m in diameter) (Hwang et al., 2017). The underestimation of small floes is mainly attributed to two factors: 1) "losing details" in the water-ice segmented image through the application of speckle filters and smoothness in KGC; and 2) a low-limit of 5 × 5 pixels for the smallest floe to be retrieved (Hwang et al., 2017). However, FSD (exponent α) derived from TS-X SAR at lower resolution was reasonably comparable with that from a higher resolution images (pixel spacing = 2.50 m) (Hwang et al., 2017).

To remove speckle noise, median (5 × 5), bilateral (half-width = 15) and Gaussian (7 × 7) filters were applied to the degraded TS-X images (pixel spacing = 8.33 m). Slight smoothness (β = 0.001) in KGC was applied to further subdue unwanted low intensity spots (caused by melt ponds) in the images, especially for early summer cases. The filtered images were then applied to the KGC algorithm to segment into water and ice regions in summer, or water, first-year ice (FYI) and multi-year ice (MYI) regions in winter (Hwang et al., 2017). Open water fraction was then calculated as a fraction of total open water pixels. Ice types between FYI and MYI were classified based on contrasting intensities between two ice types. The difference in back-scattering coefficient σ_o between FYI and MYI was typically more than 10 dB in our case. Note that ice type MYI includes second-year ice (indeed, most of the MYI in the study area is believed to be second-year ice except C4).

Next, a "floe splitting" algorithm was applied to the water-ice binary image, in order to split boundaries of touching floes. For this effort, a combination of the distance transformation, watershed and post-boundary revalidation methods was used (Hwang et al., 2017). The algorithm-produced floe split image was then manually scrutinized, by us, to check and correct the errors from the algorithm. At the end of this process, the processed image was used to calculate FSD.

2.4 Calculation of FSD

In the final error-corrected image, each ice floe pixel detected as floe boundaries was reassigned to a water pixel, and then a standard blob analysis was used to calculate floe properties for each floe. The calculated floe properties include the number of ice pixels, floe area, perimeter, major and minor axes, and the mean, maximum and minimum caliper diameters. In this study, the mean caliper diameter d is used to define floe size in FSD. The power-law exponent α was then calculated from FSD following the method described in Virkar and Clauset (2014). Following Virkar and Clauset (2014), x_{min} was estimated by minimizing the Kolmogorov-Smirnov (KS) statistic (i.e., the maximum difference in the cumulative distribution functions between the data and the power-law model that best fit the data for the region of $d \geq x_{min}$). The p-value for the goodness-of-the-fit was calculated from the KS statistics, which indicates whether the data in question is a power-law distribution or not (if p-value ≥ 0.1, it is likely a power-law distribution; otherwise not).

Note that 77% of our data passed the goodness-of-the fit test (p-value ≥ 0.1). **Figure 1b** shows a typical example of such cases. As can be seen, the blue dashed line (a representation of α) well represents the slope of the straight

line in the log-log plot of CFND. The lower bound x_{min} marks the lower limit of the straight line reasonably well. The cases (23% of the data) that fail to pass the test mostly occur in mid-August or later. Among those cases, six cases fail to pass the test even with a less conservative choice of p-value (p-value ≥ 0.05).

The failure of the test is associated with two situations. **Figure 1c** shows an example for the first situation. The blue dashed line (a representation of α) follows the slope in the log-log plot for the region between x_{min} and $d = 1000$ m, but it significantly deviates from the CFND data points beyond $d = 1000$ m. This type of situation occurs mostly in mid-August when the number of small floes suddenly increased following a substantial breakup event (see Section 5.4 and Appendix A). **Figure 1d** shows an example for the second situation. In this example, the CFND data points exhibit a curved-down line in the log-log plot. The blue dashed line follows the CFND until $d = 1000$ m, and then it significantly deviates from it. This type of situation occurs mostly in late August, when only a few large ice floes existed in a finite size of TS-X images.

3. Sea ice breakup during winter and spring
3.1 Winter (April to June 6)
a. Composition of MYI
Here "winter" is defined as a period when surface snow melt (starting from June 14) has not begun. The first TS-X images recording the state of sea ice at the MIZ clusters were acquired on April 15–21 about a month after the deployment (see **Figure 2**). These TS-X images show that the composition of MYI is slightly different between the clusters. The mean area fraction of MYI varies between 50.5% and 64.0% (**Table 1**). The lowest MYI fraction (50.5%) occurs at C2, in which MYI pieces are relatively
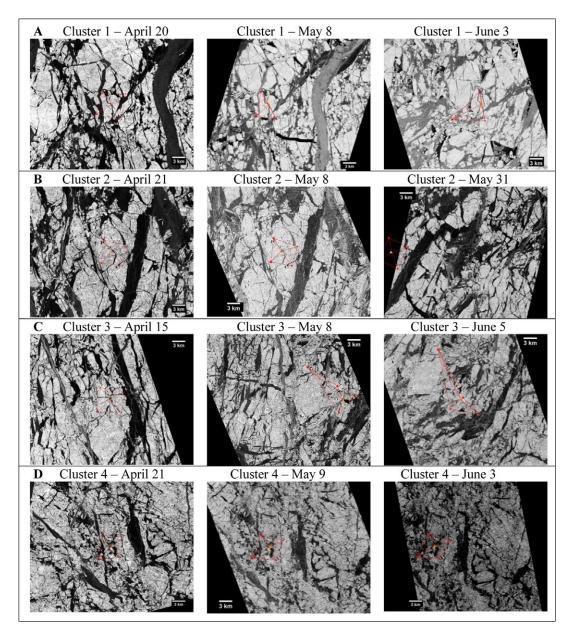

Figure 2: TS-X images showing the transition of sea ice during winter. In the image, brighter tone (white) represents MYI and darker tone (black) indicates FYI. Red symbols are the locations of buoys, and red lines are the baselines between buoys. The scale bar is 3 km; north is up in the image. DOI: https://doi.org/10.1525/elementa.232.f2

larger than at other clusters (**Figure 2B**). The mean MYI fraction is slightly higher at C1 and C3, in which MYI pieces are smaller and more fragmented than those at C2 (**Figure 2A** and **C**). The largest MYI fraction (64.0%) occurs at C4, in which MYI pieces are relatively smaller than other clusters (**Figure 2D**). Some variability (up to 4.5%) in the MYI fraction is observed over time (**Table 1**), which can be attributed to local variability (i.e., TS-X images did

Table 1: Multiyear ice (MYI) fraction retrieved from TerraSAR-X imagery of buoy clusters. DOI: https://doi.org/10.1525/elementa.232.t1

Cluster	MYI fraction[a] (%)	Period in 2014
C1	56.8 (±3.4, 5)	May 8 to June 9
C2	50.5 (±3.5, 7)	May 8 to June 9
C3	57.6 (±2.9, 6)	May 8 to June 5
C4	64.0 (±4.5, 7)	May 9 to June 6

[a] Mean (± standard deviation, n value).

not cover exactly the same area) and deformation events at C3.

b. Sea ice fracturing and deformation during winter

In winter, sea ice fracturing and deformation are observed throughout the period. When compared with April images, the May TS-X SM images at C2 and C4 show very little changes in sea ice (**Figure 2B** and **D**), except that the buoy array and surrounding sea ice at C4 are slightly rotated clockwise (**Figure 2D**). However, some changes in sea ice are observed at C1 and C3 (**Figure 2A** and **C**). First, a number of openings suddenly appear at C1 (**Figure 2A** – May 8), which are likely caused by sea ice fracturing. Second, the buoy array at C3 is stretched and its surrounding sea ice was re-arranged (**Figure 2C** – May 8), indicating strong deformation events at C3.

Between April and early May, two strong wind events are observed (w1 and w2 in **Figure 3**). During wind event w1, a strong wind was felt across all the clusters, with the peak wind speed up to 13.3 m s^{-1} (**Figure 3b**). During that time, a temporary increase (about 3–4%) in open water
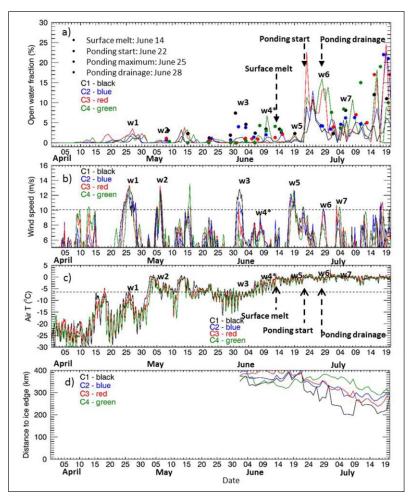

Figure 3: Evolution of sea ice and atmospheric conditions during winter-to-spring transition. The evolution of **(a)** open water fraction, **(b)** wind speed, **(c)** air temperature and **(d)** the distance from clusters to the nearest ice edge during winter-to-spring transition. In panel (a), the solid lines and closed circles are the open water fractions derived from AMSR-2 and TS-X data, respectively, at each cluster. In panel (b), solid lines are the wind speeds from ERA interim data at each cluster. In panel (c), solid lines are the air temperatures from AWS at each cluster (air temperature data from C2 are not shown here). In all panels, black, blue, red and green colors represent C1, C2, C3 and C4, respectively. Wind events (such as w1, w2…) are marked in the plots. DOI: https://doi.org/10.1525/elementa.232.f3

fraction (from AMSR-2) occurred across all the clusters (**Figure 3a**). During wind event w2, a similar opening of the ice did not occur (**Figure 3a**), although TS-X image at C1 shows a large number of openings in the May 8 image (**Figure 2A**). The strong deformation at C3 (**Figure 2C**) likely occurred during wind events w1 and w2, based on the analysis of temporal evolution of the displacement of the buoys at C3 (not shown here); i.e., one of the buoys moved from the center buoy by 10 km (initially about 4 km at the deployment) during wind event w1, and further by 14 km during wind event w2.

Next, fracturing of sea ice at the clusters is observed during early June (still before surface melt) (June images in **Figure 2**). During this time, another strong wind event (w3) occurred. The peak wind speed is 12.8 m s^{-1} at C1, but is significantly less (7.4 ms^{-1}) at C4 (**Figure 3b**). TS-X SM images, acquired during or right after this wind event, show clear evidence of fracturing at C1–C3 (June images in **Figure 2**). In **Figure 4**, fracturing (marked as "F" in the figure) between two dates is very evident, as MYI pieces located at the top-left of the image moved to the south during the wind event. Note that the fracturing is a locally forced event, as the nearest ice edge is more than 300 km away from the clusters in early June (**Figure 3d**), corresponding to small openings of open water areas in the Mackenzie Bay and in the coast of the Banks Island (see Video S1). These small openings have the potential for wave development and hence wave-induced break-up; however, we can confirm that at this time no waves were felt by any of the WBs in the clusters.

3.2 Spring breakup during surface snow melt (June 10–15)

TS-X SM images acquired on June 14–15 are shown in **Figure 5**. When compared with TS-X images acquired in early June (see **Figure 2**), a significant change in TS-X backscattering coefficient (σ_o) is observed. During this time, TS-X σ_o of sea ice decreased almost by 12 dB at the buoy locations (compared between May 8 and June 14 for

the range of incident angle of 23–24°). This significant decrease in TS-X σ_o can be attributed to high water content (i.e., funicular regime) in the wet snow (Onstott, 1992; Hwang et al. 2007), indicating that the onset of snow melt occurred around June 14 at the clusters. This timing of snow melt coincides with the rise of air temperature to 0°C on June 10 from –8°C on June 5 (**Figure 3c**). Note that there were two warming periods in May (around May 1 and 13) in which air temperature increased to 0°C (**Figure 3c**), but no significant changes in TS-X σ_o values are observed.

During this surface melt transition, the wind speed was moderate compared to other earlier wind events; e.g., the mean wind speed was 6 m s^{-1}, with the peak wind speed up to 9.3 m s^{-1} at C1. Very little change in open water fraction (from TS-X) is observed across the clusters; i.e., the open water fraction changed by 0% at C1, 0.6% at C2, 1.2% at C3 and 1.1% at C4 (**Figure 3a**). Despite the very small change in open water fraction, surface snow melt marks a very important transition. The surface melt coincides with a warming of the mean ice temperature to above –3°C (based on IMB data). Brine volume of sea ice increases sharply above ice temperature of –5°C (Cox and Weeks, 1983), and the strength of sea ice is strongly correlated to brine volume (Weeks, 1998). As a result, sea ice, especially FYI formed in leads or cracks in later winter, is more susceptible to breakup with the same internal pressure. The effects can be further intensified during melt ponding and drainage followed by the surface melt, as the mean ice temperature further increases to –1°C. Melt ponding weakens the ice because of increased solar absorption leading to localized thinning and degradation of the internal structure, so the ice is more susceptible to fracture.

To demonstrate this point, a sequence of TS-X images (zoomed into a floe) are shown in **Figure 6**. First, note that the distinction in TS-X σ_o values between MYI and FYI is very evident in a winter (before surface melt) condition (**Figure 6a**). During the surface melt (June 14), open
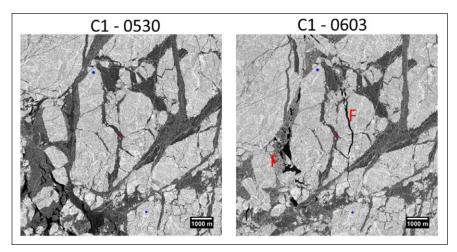

Figure 4: Close-up TS-X SM images acquired before and after wind event w3 at C1. Red and blue symbols represents the location of center buoy and surrounding buoys. The red letter "F" marks the fracturing during the wind event. The date of the image is shown on the top of each image (i.e., "0530" and "0603" mean May 30 and June 3 in 2014, respectively). Scale bar is 1000 m. DOI: https://doi.org/10.1525/elementa.232.f4
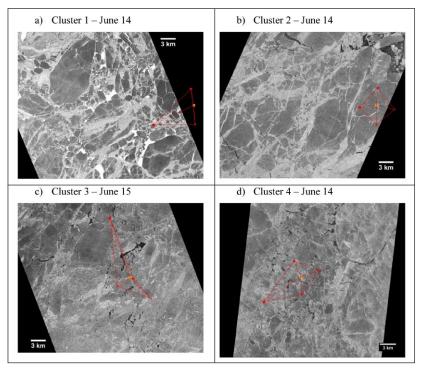
Figure 5: TS-X images showing the transition of sea ice during spring melt. In **(a)**, the brightest tone (whitest) represents open water areas due to high TS-X backscattering σ_0 from wind-roughened ocean surface. In all images, MYI appears darker than FYI, due to the reversion in TS-X σ_0 in spring melt. Red star symbol with yellow rectangle represents the location of the buoy at the centre of each cluster. Four red symbols surrounding the centre buoy represent the location of the buoys deployed at four corners of the cluster (northeast, northwest, southwest and southeast). Scale bar is 3 km; north is up in the image. DOI: https://doi.org/10.1525/elementa.232.f5
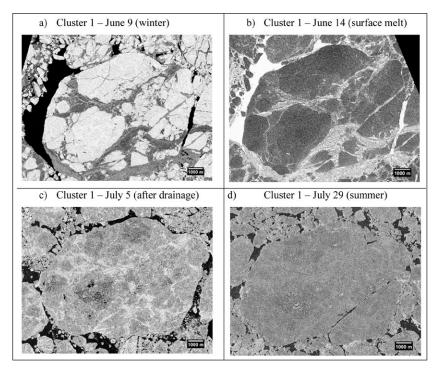

Figure 6: TS-X images showing the transition of sea ice from winter to summer. A small section of TS-X SM images acquired on June 9 (winter), June 14 (surface melt), July 5 (after melt pond drainage) and July 29 (summer) at C1. In **(a)**, the brightest tone (white) represents MYI, the darker tone (grey) indicates FYI, and the darkest tone (black) is open water. In **(b)**, the backscattering intensity was reversed. The brightest tone represents open water (high backscatter from wind-roughened sea surface). The darker tone represents MYI, while the grey tone represents FYI and thin refrozen leads. In **(c)**, the darkest tone is open water, and the brighter grey tone is FYI or used-to-be leads. Black spots on sea ice are melt ponds on MYI that survived the drainage. Scale bar is 1000 m; north is up in the image. DOI: https://doi.org/10.1525/elementa.232.f6

water areas exhibit higher TS-X σ_o from wind-roughened sea surfaces (**Figure 6b**). Inversion between MYI and FYI σ_o also occurs this time (Onstott, 1992), and now thinner FYI is shown in brighter tone. Later during the melt pond drainage and summer breakup, floe breakup occurs along those bright toned (thinner) ice areas (**Figure 6c** and **6d**). Here note that some melt ponds on MYI still appear in TS-X images after the melt pond drainage in June (**Figure 6c**), but most of them have disappeared in TS-X images in late July (**Figure 6d**). During the snow melt, the distance to the ice edge remained almost the same as before (i.e., >300 km) (**Figure 3d**).

3.3 Spring breakup during melt ponding (June 25) and drainage (June 28)

The major transition between mid-June and early July is the formation and drainage of melt ponds on the surface of sea ice, and the appearance of more distinctive sea ice floes (**Figure 7**). Based on WB 6-hourly webcam photographs, the maximum extent of melt ponds for all clusters is estimated to have occurred around June 25 and the drainage of these melt ponds a few days later. Although this period was not well covered by the TS-X data (**Figure 3a**), TS-X images acquired in late June or early July clearly show low intensity (dark) areas due to the presence of melt ponds (**Figure 7**).

During this two-week period, a significant increase of open water fraction is observed. Across the clusters, the TS-X open water fraction increased by 2.6–4.7% for that period (**Figure 3a**). The AMSR-2 open water fraction shows an even more dramatic increase (up to 24%) during June 22–25 (**Figure 3a**). We speculate that this dramatic increase in open water fraction is likely due to widespread surface water during melt ponding (not open water resultant from floe breakup), which can significantly affect passive microwave signatures at AMSR-2 operating frequencies (Hwang et al., 2007). As TS-X images were not available during melt ponding, it is difficult to assess how melt ponding may have affected AMSR-2 open water fraction. During this period, the distance to the ice edge remained larger or around 300 km from the clusters (**Figure 3d**). Note that there are some low values in the distance to the ice edge for C1 during June 22 to July 10. These values correspond to the detection of the nearest ice edge in a small inlet that is connected to a large open water area in the west of the Alaska (see Video S1).

4. Summer FSD transition (July–August)
4.1 Overall transition of open water fraction and FSD in summer

Figure 8 shows the temporal evolution of open water fraction, power-law exponent α, total floe number density (TFND), wind speed and the distance to ice edge between July and August. Until mid-July, open water fraction remained around or below 10% with relatively small fluctuations (**Figure 8a**). This relatively low open water fraction can be attributed to the fact that all clusters are located far away from the ice edge during this time (>200 km) (**Figure 8e** and **Figure 9a**) and that ice field was not under significant wind forcing or stress that would drive significant ice divergence.
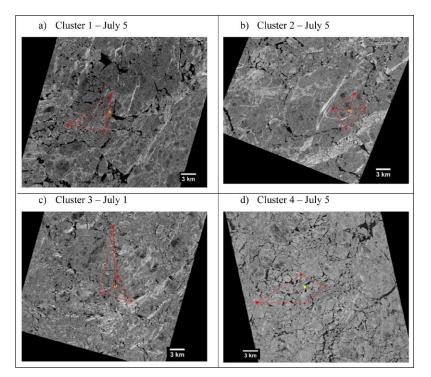

Figure 7: TS-X images showing early summer breakup of sea ice. TS-X images shown above were acquired between July 1 and 5 at MIZ clusters. In the images, the darkest tone is open water, and brighter grey tone is sea ice. Black spots on sea ice are melt ponds. Red star symbol with yellow rectangle represents the location of the buoy at the centre of each cluster. Four red symbols surrounding the centre buoy represent the location of the buoys deployed at four corners of the cluster (northeast, northwest, southwest and southeast). Scale bar is 3 km; north is up in the image. DOI: https://doi.org/10.1525/elementa.232.f7
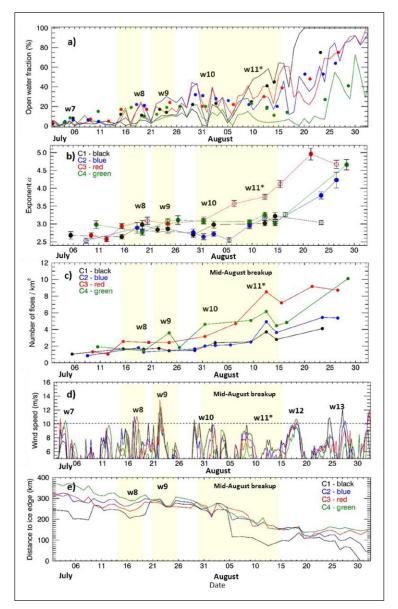
Figure 8: Evolution of sea ice and atmospheric conditions during summer. The evolution of **(a)** open water fraction, **(b)** power law exponent α, and **(c)** total floe number density (TFND), **(d)** wind speed, and **(e)** the distance from clusters to the nearest ice edge during summer (July to August). In panel (a), the solid lines and closed circles are the open water fractions derived from AMSR-2 and TS-X data, respectively, at each cluster. In panel (b), solid lines with closed circles are α values for p-value ≥ 0.1 (valid for the power-law), while the data points with open circles are α values for p-value < 0.1 (not valid for the power-law). The error bars at each circle are the error estimate for α. In panel (d), solid lines are the wind speeds from ERA interim data at each cluster. In all panels, black, blue, red and green colours represent C1, C2, C3 and C4, respectively. Wind events (such as w1, w2…) are marked in the plots. In plots in panels (b), α and p-value were calculated following Virkar and Clauset, (2014). DOI: https://doi.org/10.1525/ elementa.232.f8

From mid-July, open water fraction shows more fluctuations with an overall increasing trend (**Figure 8a**). In August, the biggest change in open water fraction occurs at C1, which quickly increases from August 5 and reaches almost 100% by August 20 (within two weeks) (**Figure 8a**). This rapid increase in open water fraction at C1 coincides with a sharp decrease in the distance to the ice edge on August 5 (from 250 km to 100 km) (**Figure 8e**), corresponding to the rapid expansion of open water area in the north of the Alaska (see Video S1). Open water fraction at C2–C3 gradually increases throughout August,

reaching almost 100% at the end of August (**Figure 8a**). Open water fraction at C4, however, remains lower than 20% until August 24, and then quickly increases to about 70% within a week (**Figure 8a**). For C2–C4, the distance to the ice edge gradually decreases during August, reaching almost 50 km for C2 while 150 km for C3 and C4 on September 1 (**Figure 8e**, **Figure 9**).

FSD is derived from TS-X images starting from July 5–10 until late August (see Table S1). The results are shown as α and TFND in **Figure 8b** and **c**. As can be seen, both α and TFND values at C1 and C2 are quite comparable and remain

relatively unchanged until August 10 (**Figure 8b** and **c**); e.g., mean $\alpha = 2.84 \pm 0.15$ at C1 vs. mean $\alpha = 2.73 \pm 0.15$ at C2 (**Table 2**). (Note that the standard deviation of 0.15 is slightly larger than the mean α error of 0.1.)

Table 2: Power law exponent (α) and total floe number density (TFND) for buoy clusters between July 5 and August 10 in 2014. DOI: https://doi.org/10.1525/elementa.232.t2

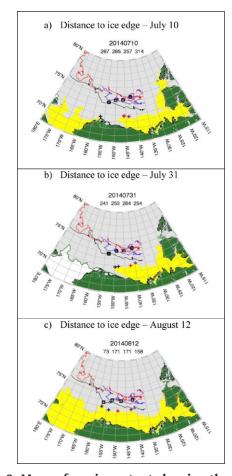| Cluster	α^{a}	TFND^{a} (km^{-2})	n
C1	2.84 ± 0.15	1.74 ± 0.49	8
C2	2.74 ± 0.15	1.79 ± 0.53	8
C3	2.99 ± 0.33	2.53 ± 1.21	7
C4	3.01 ± 0.13	3.07 ± 1.57	6

^{a} Mean ± standard deviation.

Figure 9: Maps of sea ice extent showing the nearest ice edge to the buoy clusters. Daily ice extent map overlaid with GPS trajectories of the reference buoys of C1 (black), C2 (blue), C3 (red) and C4 (purple). The location of the buoy for that date is marked by an open square symbol. The cross symbols mark the location of the nearest ice edge for the corresponding cluster. The yellow coloured area represents the open water area that is connected to the nearest ice edge. The four numbers on the top of each image are the distance to the ice edge for C1 (left) to C4 (right) in kilometres (e.g., "73 171 171 158" represent that the distance to the ice edge for C1, C2, C3, and C4 are 73 km, 171 km, 171 km, and 158 km). DOI: https://doi.org/10.1525/elementa.232.f9

Compared to these values at C1 and C2, both α and TFND values at C3 and C4 are higher and more variable (**Table 2**). This difference can be explained by the following.

· First, the increase in α is potentially caused by the floe breakup during the wind event or/and some spatial variability in FSD (especially for C3). At C3, TS-X images acquired on July 15 and 20 shifted their centers to the west of the buoy cluster, while TS-X images acquired on July 9 and 12 were centered on the east of the buoy cluster. The overlapping area between these two images was very small (less than 10 %).
· Second, both α and TFND steadily increased from July 24 until late August (**Figure 8b** and **c**). In fact, α values at C3 are consistently higher by 0.3–1.0 (which is much larger than the mean α error of 0.1) than at other clusters for that period.
· Third, α values at C4 increased by 0.31 between July 19 and 24, and then maintain the value until August 9 (**Figure 8b**).

Another point to make in terms of α and TFND is a notable transition in mid-August. Both α and TFND show a steep increase in those values between late July and mid-August, although the level of increase varied between the clusters (**Figure 8b** and **c**). For the summer transition, increasing α corresponds to a decrease of mean floe size D (a mean of d for each case), summarized in a hyperbola equation (see Appendix D).

4.2 Response to mid-July wind event w8 (July 14–17)
During a strong wind event (w8, July 14–17), the peak wind speed was measured to be 10.5–11.1 m s^{-1} at C1–C3 (**Figure 8d**). In response to this wind event, the AMSR-2 open water fractions show some fluctuations except at C1, which remains unchanged throughout this wind event (**Figure 8a**).

Overall changes in α and TFND during this wind event are very moderate: α and TFND increased by 0.15–0.28 and 0.07–0.44, respectively, for C1–C3, while α and TFND decreased by 0.21 and 0.48, respectively, for C4 (**Table 3**). These changes in α are slightly higher than the mean α error of 0.1, indicating a moderate floe breakup. Note that the coverage of the TS-X images was only slightly off between the two dates (**Figure 10**), suggesting that the two images reasonably represented almost the same floe samples unless significant spatial variability occurred in FSD.

The degree of floe breakup is relatively low at C1 and C3; i.e., the increase in α and TFND (**Table 3**) was moderate and CFNDs showed no clear crossover (intersection) between the two dates during the wind event (**Figure 11A**; not shown for C3). No clear visual evidence for the floe breakup can be seen from the corresponding TS-X images (**Figure 10A**; not shown for C3). The images also show no clear increase in the number of small floes ($d = 100$–500 m) nor decrease in the number of large floes ($d > 1600$ m) (**Figure 11A**; not shown for C3).

A higher degree of floe breakup can be seen from C2 in which the increase in α and TFND is the largest

Table 3: Changes in power law exponent (α) and total floe number density (TFND) during mid-July wind event (w8). DOI: https://doi.org/10.1525/elementa.232.t3

Cluster	Period in 2014[a]	$\Delta\alpha$	ΔTFND (km^{-2})	Image overlap[b]
C1	July 15–22	0.20	0.07	Slightly off
C2	July 8–19	0.28	0.44	Slightly off
C3	July 15–20	0.15	0.12	Same area
C4	July 10–19	−0.21	−0.48	Slightly off

[a] As framed by satellite images available on the two dates given.
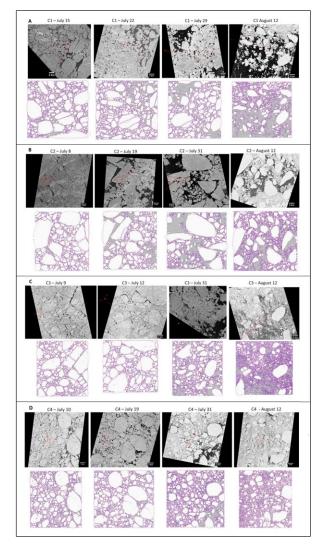[b] Description of how well the two images overlap each other.

Figure 10: TS-X images and corresponding "floe maps" showing summer floe breakup. Snapshot of TS-X images and corresponding floe maps for selected dates in July and August. For each panel, TS-X images are shown in a UTM coordinate, and the location of buoys are marked in red and yellow symbols connected with red lines. In floe maps, ice floes are shown in white, and floe boundaries in red. Blue ellipses are elliptic fits of the detected floes. Floe maps were derived by using the algorithm described in Hwang et al. (2017). DOI: https://doi.org/10.1525/elementa.232.f10

(**Table 3**). The corresponding TS-X images show direct (visual) evidence of floe breakup during this wind event: a large floe on which the center buoy was deployed is broken into three floes between July 8 and 19 (compare the July 8 image with the July 19 image in **Figure 10B**). Note that the breakup of the floe occurs along the fracture lines (shown as brighter tone lines in the July 8 image). Of particular interest is that those fracture lines are refrozen leads or cracks that were formed in previous winter and spring, which appear in brighter tone (whiter) after melt pond drainage (see Section 4). FND also shows an increase in the number of small floes (d = 100–500 m), and a decrease in the number of large floes ($d > 1600$ m) (**Figure 11B**).
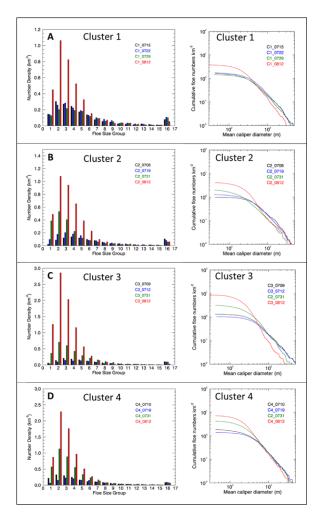
At C4, α and TFND decreased by 0.21 and 0.48 km^{-2}, respectively, during the wind event (**Table 3**). The

corresponding TS-X images and FND show that the number of large floes ($d > 2000$ m) increased slightly between the two dates (compare the July 10 image with the July 19 image in **Figure 11D**), so the potential role of wind in the changes observed in this cluster is less clear, as the increase in the number of large floes indicates that the two images comprised slightly different ice floe samples.

As can be seen above, breakup (caused by local wind forcing) is most evident at C2 (with some visual evidence from the TS-X images) among the clusters during the wind

event (w8). There is an indication that breakup might occur at C1 and C3 (based on slight increase in α), but based on the results mentioned previously it is difficult to ascertain. No apparent breakup is observed at C4.

4.3 Response to late July wind event w9 (July 21–22)
During a stronger wind event (w9, July 21–22), the peak wind speed was 13.5 m s^{-1} (**Figure 8d**). The clusters respond differently to the wind event (w9). It shows a decrease in α by 0.14–0.17 at C1 and C2, but an increase

Figure 11: Transition of floe size distribution during summer. Floe number density (FND) and cumulative floe number density (CFND) plots for selected dates at C1–C4. Floe size group is as follow: group 1 is for 0 m ≤ d < 100 m, group 2 is for 100 m ≤ d < 200 m…, group 16 is for d ≥ 1600 m. DOI: https://doi.org/10.1525/elementa.232.f11

Table 4: Changes in power law exponent (α), total floe number density (TFND) and area fraction of small (F_S, < d_{inter}) and large (F_L, ≥ d_{inter}) floes during late July wind event (w9). DOI: https://doi.org/10.1525/elementa.232.t4

Cluster	Period in 2014[a]	$\Delta\alpha$	ΔF_S (km^{-2})	ΔF_S (%)	ΔF_L (%)	d_{inter}[b] (m)	Image overlap[c]
C1	July 22–29	−0.14	−0.26	n/a[d]	n/a	n/a	Slightly off (dispersed)
C2	July 19–31	−0.17	0.72	1.0	−11.6	250	Slightly off
C3	July 12–31	0.53	2.11	30.6	−29.7	900	Slightly off (dispersed)
C4	July 19–31	0.30	3.18	11.0	−21.9	800	Slightly off

[a] As framed by satellite images available on the two dates given.
[b] Point in the mean caliper floe diameter d where the two cumulative floe number densities intersect each other.
[c] Description of how well the two images overlap each other.
[d] Not available.

in α by 0.30–0.53 at C3 and C4 (**Table 4**). The decrease in α at C1 is accompanied with the decrease in TFND, yet the decrease in α at C2 with the increase in TFND (**Table 4**). Note that AMSR-2 open water fraction shows an increase by 20% at C1 and by 30% at C2 during the wind event. TS-X images show very dynamic and diverging ice condition at both C1 and C2 after the wind event (see July 29 in **Figure 10A** and July 31 in **Figure 10B**). Despite such a dynamic ice condition, no increase in α is observed at C1 and C2.

The responses at C3 and C4 to the wind event (w9) are very different. Both α and TFND at C3 and C4 increased by 0.30–0.53 and 2.11–3.18 km^{-2}, respectively (**Table 4**), indicating breakup events at the cluster locations. Increased number of smaller floes is also clearly visible from the corresponding TS-X images at the end of July at C3 and C4 (compare the July 12 image with the July 31 image in **Figure 11C** and compare the July 19 image with the July 31 image in **Figure 11D**). Note that the July 12 image at C3 was used instead of the images acquired right before the wind event (w9) (e.g., July 15 or 20), as the coverage of the July 12 image provided much better overlap with the July 31 image. Thus, the difference at C3 includes both wind events w8 and w9. However, note that the breakup was not obvious at C3 during the wind event w8 (see Section 5.2).

For C3 and C4, the crossover (intersection) in CFNDs can be identified between the two dates, although the crossover is less clear at C4 (compare the July 12 image with the July 31 image in **Figure 11C** and the July 19 image with the July 31 image in **Figure 11D**). The intersection occurs at about 900 m for C3 (d_{inter} = 900 m) and 800 m for C4 (d_{inter} = 800 m) (**Table 4**). The change in area fraction across the intersection can provide information on the balance between supply and removal of broken floes. For C3 the decrease of the area fraction of large floes ($\Delta F_L \geq d_{inter}$) is almost balanced with the increase of the area fraction of small floes ($\Delta F_L \geq d_{inter}$) (**Table 4**). This near balance indicates that the increase of smaller floes ($d < d_{inter}$) would be supplied by the breakup of larger floes ($d \geq d_{inter}$). For C4 ΔF_S is unbalanced with ΔF_L (**Table 4**). The increase of smaller floes ($d < d_{inter}$) only accounts for the half of the potential supply by the breakup of larger floes ($d \geq d_{inter}$). The cause of this unbalance is not clear. The removal of small floes can occur through melting, advection or other processes. We speculate that this unbalance may be attributed to the lack

of the algorithm to detect small (closely packed) floes (Hwang et al., 2017). The nearest ice edge during this period was further away from the clusters (>250 km) (**Figure 8e**). Thus, it is unlikely that the breakup is due to a remotely forced event (for example, the WBs see no evidence of swell).

As shown above, the decrease in α at C1 and C2 apparently indicates no breakup in the areas (**Table 4**), despite of more dynamic ice conditions at C1 and C2 (**Figure 8a**). For C2 the crossover (intersection) of two CFNDs occurs around 250 m (**Figure 11B**). For that crossover, ΔF_S is largely unbalanced with ΔF_L (**Table 4**), which suggests that a significant portion of small floes would be removed through melting and advection. Typically, the scale at which lateral melting processes is thought to be important is for floe sizes smaller than about 30 m (Steele, 1992), though mixing at the edges of comparatively large floes (like those from 200–700 m identified here) could cause rapid melting (Horvat et al., 2016). Note that, by the end of July, oceanic heat flux measured at C2 show a rapid increase up to 30 Wm^{-2} (see Section 6.2). The analysis of buoy data also shows that significant divergent ice motion occurred during late July (not shown here). Thus, we speculate that the decrease in α at C1 and C2 is likely due to faster removal of smaller floes by the processes mentioned above.

Above results suggest that the floe breakup clearly occurs at C3 and C4 during the wind event (w9), in which the increase of smaller floes ($d < \sim800–900$ m) is supplied by the breakup of larger floes ($d \geq \sim800–900$ m). We speculate that the floe breakup may also occur at C1 and C2. However, the removal of smaller floes (by melting, advection or other processes) may exceed the supply of smaller floes from the breakup of larger floes, which causes no obvious increase (or even decrease) in α at C1 and C2 during the wind event (w9).

4.4 Mid-August transition

A very distinctive FSD feature in August is a significant increase in α and TFND during mid-August, which occurs simultaneously across the clusters, but at a variable magnitude. Between July 29 and August 12, α values at the clusters are increased by 0.19–0.66 (**Table 5**). These increases are much larger than the mean α error of 0.10. Similar increases in TFND are also shown in **Table 5**. These increases are much larger than what was observed during wind events in July (**Table 3** and **Table 4**), except

Table 5: Changes in power law exponent (α), total floe number density (TFND) and area fraction of small (F_S, $< d_{inter}$) and large (F_L, $\geq d_{inter}$) floes leading to mid-August breakup. DOI: https://doi.org/10.1525/elementa.232.t5

Cluster	Period in 2014[a]	$\Delta\alpha$	ΔTFND (km^{-2})	ΔF_S (%)	ΔF_L (%)	d_{inter}[b] (m)	Image overlap[c]
C1	July 29–August 12	0.32	2.24	7.2	−27.3	500	Slightly off (dispersed)
C2	July 31–August 12	0.52	2.93	13.4	−8.1	900	Dispersed
C3	July 31–August 12	0.66	5.35	15.6	−29.1	500	Slightly off (dispersed)
C4	July 31–August 12	0.19	1.54	9.2	−9.1	600	Almost same area

[a] As framed by satellite images available on the two dates given, leading to mid-August breakup.
[b] Point in the mean caliper floe diameter d where the two cumulative floe number densities intersect each other.
[c] Description of how well the two images overlap each other.

C4. More importantly, they occur simultaneously across the clusters (**Table 5**).

TS-X images acquired on August 12 at C1–C4 clearly show sudden increase in smaller floes, which did not appear in the July images (**Figure 10**). The increase in small floes is also very evident in the plots of FND and CFND (**Figure 11**). The August 12 CFND at C1 intersects the July 31 CFND at d_{inter} = 500 m, indicating large ($d > 500$ m) floe breakup into small ($d < 500$ m) floes (**Figure 11A**). At C2, the August 12 CFND intersects the July 31 CFND at d_{inter} = 900 m, but the number of very large ($d > 2000$ m) floes is almost unchanged between July 31 and August 12 (**Figure 10B**). At C3, the August 12 CFND intersects the July 31 CFND at d_{inter} = 500 m, similar to the C1 case (**Figure 11C**). At C4, the August 12 CFND intersects the July 31 CFND at d_{inter} = 600 m.

ΔF_L values at C1 and C3 are larger than those values at C2 and C4 (**Table 5**), suggesting more breakup of large floes at C1 and C3 across the intersection. Note that, by August 12, open water fraction increased to 60% at C1, to 40% at C3, to 30% at C2 or decreased below 10% at C4 (**Figure 8a**). These changes indicate that the larger ΔF_L values at C1 and C3 are likely associated with rapid opening (diverging ice condition) at those locations, and the lower ΔF_L value at C4 with closing (converging ice condition) at that location. The small ΔF_L value at C2 is likely due to the presence of very large floes ($d > 3000$ m) that survived throughout mid-August (**Figure 10B**), which delays the breakup at that location.

ΔF_S and ΔF_L are unbalanced at C1–C3, with C4 as the exception (**Table 5**). For C1 and C3, the increase of the smaller floes (ΔF_S) is lower than the decrease of larger floes (ΔF_L) by about 10–14%. This difference suggests that some smaller floes could be removed through melting, advection and other processes, associated with much more dynamic and divergent ice conditions at C1 and C3 (**Figure 8a**). Note also that the distance between the ice edge and C1 is quickly reduced during this period (**Figure 8e**). For C2 the increase of the smaller floes (ΔF_S) is higher than the decrease of larger floes (ΔF_L) by about 5% (**Table 5**). The cause of this unbalance is not clear. We speculate that this unbalance is partly due to the survival of very large floes ($d > 3000$ m) as well as an addition of small floes through advection. For C4 the increase of smaller floes (ΔF_S) is balanced with the decrease of larger floes (ΔF_L). This finding indicates that the smaller floes created by the breakup of larger floes are not removed from the area, due to relatively less dynamic ice condition at that location (**Figure 8a**).

5. Discussion
5.1 Effects of spring deformations on FSD at Cluster 3
In Section 5, it was found that α and TFND at C3 were consistently higher than other clusters (**Figure 8b** and **c**). In particular, the increase in α at C3 in August was much steeper than what was observed at other clusters; i.e., α at C3 reached up to 4.96 on August 21 (**Figure 8b**). TFND also shows much higher values and steeper increases in August (**Figure 8c**). These findings raise a question – what

causes such difference in FSD at C3? One distinctive difference observed at C3 is the occurrence of strong deformation events. At least two strong deformation events at C3, the first in late April and the second in early June, were observed from TS-X images and *in-situ* buoy data. Both deformation events were strong enough to considerably re-arrange sea ice at C3. To demonstrate this point, a sequence of TS-X images (enlarged to a 10 km scale centered at the buoy array) are shown in **Figure 12**. The image in April shows that MYI floes are relatively large, and no apparent fracturing in FYI (**Figure 12a**). In May and June, as the deformations occurred, the buoy array rotated clockwise and stretched. During the first deformation, the buoy at the southwest corner of the array (red square symbol in **Figure 12a**) was stretched up to 14 km from the center buoy; i.e., it was stretched outside the 10-km image after the deformations (**Figure 12b** and **c**).

In **Figure 12**, some of MYI floes are marked to identify changes in sea ice during deformations. Here notable changes due to deformations are as follows:

- Deformation events created much more fracturing in FYI. For example, an area of FYI to the east of "floe 1" in the May 8 image shows very significant fracturing in the area (**Figure 12b**). Similar fracturing of FYI is shown in the June 5 image (**Figure 12c**), in which the area of FYI in the south of "floe 1" is significantly fractured during the second deformation. This fracturing leads to the breakup of the ice into distinctive floes later during summer (**Figure 12d**).
- Deformation events created more separation between MYI floes. A space between "floe 2" and "floe 3" was widened during the second deformation (**Figure 12c**). Having thinner (refrozen) ice in that area, a fracture preferably occurs in that area during summer (**Figure 12d**).
- Deformation created smaller MYI floes. For example, an area of small MYI floes was developed during the second deformation event (see the area within the red box in **Figure 12c**). These small MYI floes were later broken into individual floes around the time of the onset of surface melt (**Figure 12d**).

Additional evidence that the composition (size and distribution) of MYI floes affects summer FSD can be found in C4. Recall that α and TFND at C4 were consistently higher than at C1 and C2 (**Figure 8b** and **c**). Note that C4 was initially located northernmost among the clusters, and stayed in interior ice pack until August 12 (**Figure 9c**), and thus the persistence of larger floes at C4 was expected. One notable difference at C4 is the presence of smaller and more broken up MYI pieces in winter. No significant deformation was observed during our observations, thus the exact causes of smaller and more broken MYI pieces are unknown. Nonetheless, the examples at C3 (**Figure 12**) suggest that smaller, more broken MYI pieces could provide a more favorable condition for floe breakup in spring and summer.

In order to provide more quantitative evaluation, MYI FSD was derived from the fraction of the images consisting

of only MYI in winter. For consistency, the same algorithm parameters were used for the retrieval of MYI FSD across the clusters. As shown in **Table 6**, MYI α and N values at C3 and C4 are higher than those at C1 and C2. These higher α and N values indicate a higher potential for floe breakup in spring and summer, leading to higher α in summer, as discussed above. However, note that p-values of the goodness-of-fit for power law are smaller than 0.1 at C1 and C3 (**Table 6**), so that the validity of the power-law (scale invariant) may be in doubt for C1 and C3. Examining MYI FSD in FND and CFND plots, a large number of small MYI pieces occur at C4, similar to α. FNDs and CFNDs between C1 and C3 are relatively similar (although CFND at C3 is slightly steeper) (**Figure 13**). This similarity suggests that MYI pieces at C4 were substantially smaller than at other clusters, while the size of MYI pieces is similar between C1 and C3.

The above results highlight the two discussion points.

· Smaller MYI at C4 in winter (higher MYI α in **Table 6** and steeper CFND slope in **Figure 13**) is associated with higher α and TFND in summer at C4 (**Figure 8b** and **c**). This association suggests that smaller MYI would lead to faster and enhanced summer breakup, given other conditions being the same (e.g., the first-year ice welding MYI is in the same thickness).

· CFND and FND between C1 and C3 are relatively similar for MYI (**Figure 13**), indicating that summer breakup would be similar between C1 and C3 based on the results mentioned above. However, the summer breakup is far more intense at C3 than at C1 (high α and TFND in **Figure 8b** and **c**). This difference highlights the importance that deformation events in winter/spring may have on summer floe breakup.

Note that the boundaries of MYI floes are much more difficult to delineate, and that floe breakup does not always occur along the boundaries of MYI floes. Although MYI FND and CFND between C1 and C3 are similar, this similarity does not fully account for the effects of fracturing
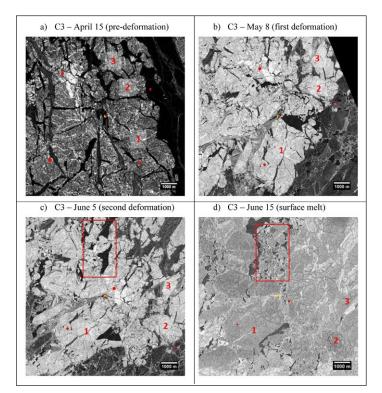

Figure 12: TS-X images showing the effects of deformation on sea ice breakup. TS-X images were taken on **(a)** April 15 (before deformation), **(b)** May 8 (after first deformation), **(c)** June 5 (after second deformation), and **(d)** June 15 (during surface melt). Scale bar is 1000 m. DOI: https://doi.org/10.1525/elementa.232.f12

Table 6: Power-law exponent (α) and lower bound of power law behavior (x_{min}) derived from multiyear ice (MYI) floes in early June. DOI: https://doi.org/10.1525/elementa.232.t6

Cluster	Date in 2014	α[a]	x_{min} (m)[a]	p-value[a]	N[b]
C1	June 3	2.64	385	0.000	2719
C2	June 5	2.84	568	0.611	1891
C3	June 5	3.36	871	0.075	3001
C4	June 7	4.16	751	0.405	5147

[a] Calculated according to Virkar and Clauset (2014).
[b] Number of MYI floes.

of FYI at C3 by deformations. More studies are needed to draw a more robust conclusion on the relationship between MYI floes and summer FSD. So far, only a few (if any) observations or studies have been conducted to examine the size and geometry of MYI in relation to summer FSD. Our study demonstrates the need for future studies on the relationship between the composition of the ice pack during winter and its relationship to the subsequent summer FSD.

5.2 Role of thermodynamics/dynamics on mid-August breakup
Another notable feature in the evolution of summer FSD is the mid-August breakup. Between late July and mid-August, a steep increase in α and TFND was observed simultaneously across all clusters (see Section 5.4). Considering that the breakup occurred over such a large spatial scale (spanning a region of more than 400 km), a thermodynamic process may have played a role in the mid-August breakup. This speculation is supported by the fact that no significant wave energy was measured at the locations of the clusters by the WBs during the mid-August breakup (Doble et al., 2017), despite the ice edge approached the clusters within 73–171 km (**Figure 9c**). Significant wave energy (a peak wave height of 0.45 m) was measured by WBs only from September 3, which rules out any possibility that the mid-August breakup might have occurred by flexural failure of floes by ocean surface waves. It is also noted that a wind event (w11* in **Figure 8d**, peak wind speed up to 10.0 m s^{-1}) occurred between August 1 and 10, but this wind event was moderate compared to wind events in July.

Thermodynamic effects were evaluated by examining sea ice mass balance at the clusters. In the 2014 MIZ experiment, a total of 20 IMBs were deployed across the clusters, measuring sea ice mass balance of sea ice (Lee et al., 2012). **Figure 14** shows the results from one of the IMBs deployed at C2 (IMB 2014C). The ice grew by 0.14 m from its initial ice thickness of 1.82 m at the deployment in March, reaching its maximum ice thickness of 1.96 m

on May 26. Bottom and surface melt began from early June, when sea ice temperature became almost isothermal (**Figure 14a**). The oceanic heat flux (the total heat from the ocean delivered to the bottom of the ice) remained below ~15 W m^{-2} for most of June (**Figure 14b**), and total melt of the ice was only 0.16 m (**Table 7**).

In July, however, oceanic heat flux increased to ~30 Wm^{-2} (**Figure 14b**), resulting in additional bottom melt of 0.43 m (**Table 7**) (i.e., an average daily melt rate of ~1.4 cm d^{-1}). In addition, there was a surface melt of 0.17 m. Taken together, the ice thickness was reduced to 1.20 m by the end of July (**Table 7**). For the first half of August, the oceanic heat flux further increased to over 50 W m^{-2} (**Figure 14b**), resulting in an addition bottom melt of 0.23 m for the first 10 days of August (**Table 6**). This rapid ice melt resulted in the ice thickness of 0.95 m on August 10 (Gallaher et al., 2016).

Sea ice mass balance measurements from other IMBs deployed at the clusters show similar trend and magnitude among all clusters. Mean and standard deviation for total ice melt was 0.75 m ± 0.16 by August 1 and 0.90 m ± 0.16 by August 10, confirming sea ice melt occurred relatively homogeneously across the clusters (Ted Maksym, personal communication). The initial ice thickness at the deployment sites ranged between 1.3 m and 3.5 m. The ice thickness range is a function of the ice types the IMBs were deployed on. For example, ice close to the 1.3 m in thickness is FYI, whilst ice closer to the 3.5 m will be MYI. Any FYI grown within the leads or cracks during late winter would be substantially thinner than 1.3 m.

During the deployment in March, direct borehole measurements and IceBridge overflights were carried out at C2 (Cole et al., 2017). The borehole data show a range of ice thickness of 1.1–3.2 m and no significant keels (Cole et al., 2017). Considering there was almost 1-m melt of total melt by August 10, some of the thin ice (≤1 m) at the deployment would completely melt out or be very thin during mid-August. Furthermore, any FYI that had not totally melted would have been very weak,
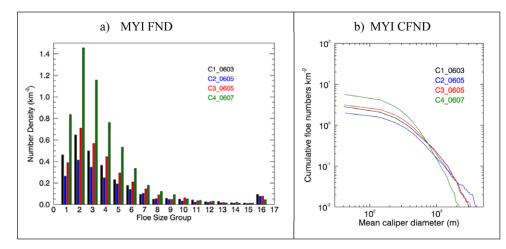

Figure 13: Comparison of MYI floe size distribution between clusters during winter. Floe number density (FND) and cumulative floe number density (CFND) derived from MYI area at C1–C4. In (a), floe size group is as follow: group 1 is for 0 m ≤ d < 100 m, group 2 is for 100 m ≤ d < 200 m…, group 16 is for d ≥ 1600 m. DOI: https://doi.org/10.1525/elementa.232.f13
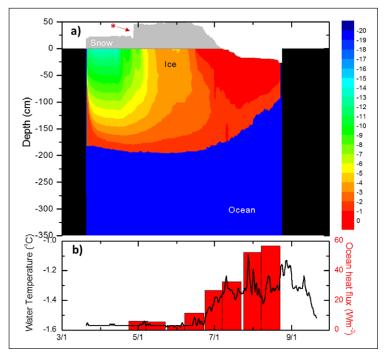
Figure 14: Evolution of sea ice and upper-ocean properties during winter-to-summer transition. Temporal evolution of **(a)** sea ice mass balance and **(b)** water temperature and oceanic heat from IMB 2014C deployed at C2. Color bar indicates temperature (°C) measured from the IMB. DOI: https://doi.org/10.1525/elementa.232.f14

Table 7: Cumulative bottom and surface melt from Ice Mass Buoy 2014C. DOI: https://doi.org/10.1525/elementa.232.t7

Date in 2014	Cumulative bottom melt (m)	Cumulative surface melt (m)	Total melt (m)	Ice thickness[a] (m)
July 1	0.16	0.00	0.16	1.80
August 1	0.59	0.17	0.76	1.20
August 10	0.82	0.19	1.01	0.95

[a] Initial ice thickness at deployment was 1.82 m; maximum ice thickness of 1.96 m was reached on May 26.

both due to its thinness and high brine content (i.e., warm temperature).

To confirm the effects of ice thickness on breakup further, GFL HRVI images acquired on July 31 and August 8 at C2 were examined (**Figure 15a** and **15b**). In the July 30 HRVI image, two large ice floes are identified (one for orange-colored polygon and the other for yellow-colored polygon in **Figure 15a**). In the August 8 HRVI image, only one of the floes (orange-colored polygon) survived, while the other floe (yellow-colored polygon) has disintegrated (**Figure 15b**). The tip of the orange-colored polygon floe has broken off, but most of the floe is still recognizable in the August 8 image. On the contrary, the yellow-colored polygon floe has been completely broken apart by August 8. An enlarged image in that area (an insert marked by a yellow box) shows small ice floes (~200 m) that consist of the remnants of ridges (elongated shapes) and ice floes with inter-connected melt ponds, which are typical in late summer condition in that region.

The question is then raised – why does such difference exist between two neighboring floes? To answer this question, two TS-X images acquired on June 5 and July 31 were compared (**Figure 15c** and **15d**). From these two images, two ice floes can be clearly identified both in HRVI and

TS-X images (note the June 5 TS-X image was rotated for the comparison). As can be seen, the yellow-colored polygon floe consists of much smaller pieces of MYI than the orange-colored polygon floe (**Figure 15c**). Also, importantly, the areas between MYI pieces are wider in the yellow-colored polygon floe than the orange-colored polygon floe. This difference is important as these areas were filled with thinner FYI and therefore are more susceptible to thermodynamic melt and weaker due to increased brine volume due to their warmer temperature.

The combination of satellite and *in-situ* buoy data as shown above suggests that sea ice thermodynamics potentially plays a significant role in mid-August breakup. Observed ice melt (~1 m) is sufficient to melt out the thinner ice that "glues" the (thicker) ice floes that survive until mid-August. This speculation is supported by the sudden increase in α and TFND in mid-August (**Figure 8b** and **8c**) and by the fact that the floe breakup occurs preferentially for the floe that consists of small pieces of MYI that are loosely congealed by thinner FYI. This reasoning is in line with "thermodynamically driven breakup" described by Arntsen et al. (2015). In fact, our results suggest that such thermodynamically driven breakup potentially plays a more significant role in the summer FSD transition.
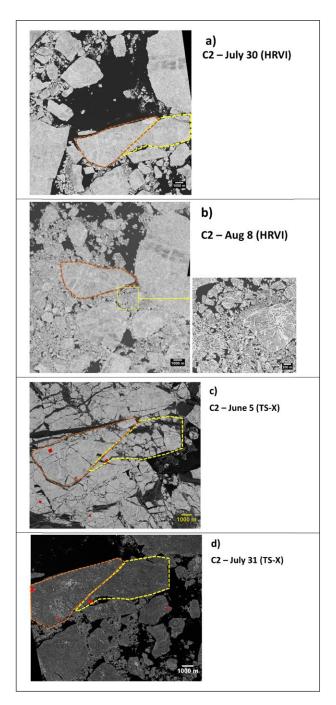
Figure 15: TS-X and HRVI images showing the breakup of an ice floe. Panels **(a)** and **(b)** show GFL HRVI images acquired on July 31 and August 8 at C2. Panels **(c)** and **(d)** show TS-X images acquired on June 5 and July 31. In (c) and (d), red symbols are the locations of the buoys. Scale bar is 1000 m, except for inset in (b) where it is 200 m. In (c), the June TS-X image has been rotated for the comparison. DOI: https://doi.org/10.1525/elementa.232.f15

If this greater role is the case, could the composition of MYI predict the status of FSD in mid-August? In **Table 6**, MYI α values estimated for C2 and C4 have sufficiently high p-values for the validity of the power-law distribution. By comparing those MYI values ($\alpha = 2.84$ at C2 and $\alpha = 4.16$ at C4) with the corresponding values in

mid-August ($\alpha = 3.07$ at C2 and $\alpha = 3.26$ at C4), one finds that MYI α is lower than mid-August α by 0.23 at C1, but it is higher by 0.90 at C4. There are a number of the reasons for the difference between MYI α and mid-August α.

· Delineating MYI floes was much more difficult to achieve than summer ice floes. Some of the thin fracture lines may not be resolved in TS-X images.
· It was difficult to account for the effects from the breakup of FYI that did not melt out by mid-August.
· MYI FSD did not represent ridges that composed a considerable part of mid-August floes, suggesting that direct comparison between MYI α and summer α is not straightforward.

6. Closing remarks

During the 2014 ONR MIZ experiment, a large number of autonomous multisensor buoys were deployed at four separate clusters in the Beaufort Sea. The large-scale ice context of these drifting buoys were continuously monitored by satellite data, including TerraSAR-X (TS-X) Synthetic Aperture Radar (SAR) and USGS GFL high resolution visible imagery (HRVI). The acquired TS-X images were analyzed to derive open water fraction, ice type and sea ice floe size distribution (FSD).

The Lagrangian view of TS-X images at MIZ clusters provided unique insight on the winter-to-summer transition of sea ice breakup and FSD. The results show that strong wind events can cause sea ice fracturing and temporarily increase in open water fraction in winter (**Figures 3** and **4**). Surface snow melt occurred in mid-June, coinciding with the rise of air temperature to around 0°C (**Figure 3**), which was evident by a decrease in TS-X backscattering coefficient (σ_o) by almost 10 dB. Surface melt marks an important transition for following reasons:

· no more refreezing of leads or cracks to form new ice,
· increase in brine volume within sea ice and associated weakening of sea ice strength, and
· the reversal of sea ice σ_o between MYI and FYI.

Surface melt was followed by melt ponding that reached its maximum on June 25 and was followed by pond drainage a few days later (**Figure 3**). This melt-ponding period was clearly marked by a sharp increase in open water fraction (from AMSR-2). This period also marks the transition to distinguishable summer ice floes (**Figures 6** and **7**).

The evolution of summer FSD was evaluated by examining the temporal evolution of power-law exponent α and total floe number density (TFND) at C1–C4. Corresponding FND, CFND and TS-X images were also used to assist the analysis. The results showed a moderate breakup at C2 during the mid-July wind event (w8) and a stronger breakup during the late July wind event (w9). During the mid-July wind event (w8), the breakup at C2 was most evident (from both α/TFND and TS-X image), but the degree of breakup was weaker than that for the late July wind event (w9). There was an indication that a "moderate" floe breakup might occur at C1 and C3 (based on slight increase in α in

Table 3), but breakup was not evident from FND, CFND or TS-X image (**Figure 10** and **11**). The results shows no sign of floe breakup at C4, which could be attributed to the lower wind speed measured at C4 (**Figure 8d**) and the fact that the cluster was the northernmost one. The exact cause for the difference observed among C1–C3 is difficult to ascertain. In speculation, the difference suggests that a mild breakup might have occurred at C1 and C3, but the breakup might have been too weak to detect.

For the late July wind event (w9), stronger breakup was evident at C3 and C4 (stronger than the mid-July event). Decrease in α indicated no apparent breakup at C1 and C2 (**Table 4**). We speculate, however, that lower α and TFND can occur if the removal of smaller floes (due to melting, advection and other processes) exceeded the supply of smaller floes from the breakup of larger floes. The breakup during the July wind events was likely induced by local wind forcing through either floe-floe interaction or/and mechanical failure by increased internal ice stress, as no significant wave energy was measured by the WBs and the nearest ice edge was still more than 200 km away from the clusters.

Two most notable features of the summer FSD evolution are:

· a consistently high α and TFND (more fragmented floes) at C3 and C4, and
· a sudden increase in α and TFND in mid-August across the clusters (i.e., mid-August breakup).

The results show that high α values at C3 and C4 in summer are likely associated with smaller MYI and strong deformation events that increased fracturing of both FYI and MYI in winter. The results show that mid-August breakup is closely related to sea ice thermodynamic processes. Observed melt rates at the clusters were sufficient to melt out thin FYI (that formed late winter or early spring) in mid-August. Thus, mid-August breakup was most likely a by-product of thermodynamic melt combined with internal stress that was able to break up the weakened ice floes in even a moderate wind.

This study highlights the challenges and promise of future modeling work. The distribution of refrozen leads/flaws within a winter floe is important for predicting the summer FSD; thus, improving the representation of winter sea ice will be useful for predicting the summer FSD. This study also demonstrates a link between summer floe breakup and sea ice melting. Accurate parameterization of sea ice melting, including the effects of melt ponds (e.g., Flocco et al., 2010, Horvat et al., 2016) is essential for predicting and evolving the summer FSD. Despite significant and fast-evolving efforts (e.g., Horvat and Tziperman 2015, 2017; Zhang et al., 2015, 2016; Roach et al., 2017; Chris Horvat, personal communication), models of the FSD are still at an early stage of development and validation, and evaluating their agreement with observations here and in other FSD studies is an important area of future work.

As a final note, the rates of deformation and thermodynamic melt of Arctic sea ice have increased in recent years, in response to the recent decrease in sea ice extent and thickness (Rampal et al., 2009; Kwok and Cunningham, 2012; Zhang et al., 2012; Stroeve et al., 2014). Our results suggest that such increases in thermodynamically driven MIZ would promote faster and more severe breakup of sea ice (i.e., smaller floes), potentially leading to lower sea ice extent in summer.

Appendix A: List of symbols and acronyms

α	Power law exponent
ΔF_L	The change in area fraction of large floes
ΔF_S	The change in area fraction of small floes
σ_0	Backscattering coefficient
A	Floe area of a floe
d	Mean caliper diameter of a floe
d_{max}	Maximum caliper diameter of a floe
d_{min}	Minimum caliper diameter of a floe
D	A mean of mean caliper diameter d for each image
N	Total number of floes
P	Floe perimeter of a floe
x_{min}	Lower-bound to the power law behavior
AFOB	Arctic Ocean Flux Buoy
AMSR-2	Advanced Microwave Scanning Radiometer-2
AWS	Automatic Weather Station
CRREL	Cold Regions Research and Engineering Laboratory
FND	Floe number density (km^{-2})
FSD	Floe size distribution
FYI	First-year ice
GFL	Global Fiducial Library
CFND	Cumulative w size number density, $N(x)$
HRVI	High-resolution visible-band image, also referred to as literal imagery derived
IMB	Ice Mass Balance Buoy
ITP-V	Ice-Tethered Profiler with Velocity
KGC	Kernel Graph Cuts
LSF	Least-square fit
MIZ	Marginal ice zone
MYI	Multiyear ice
ONR	Office of Naval Research
TFND	Total floe number density (km^{-2})
TS-X	TerraSAR-X
SAR	Synthetic Aperture Radar
SIC	Sea ice concentration
SM	StripMap mode, TerraSAR-X
SC	ScanSAR mode, TerraSAR-X
WB	Wave Buoy

Appendix B: A brief note on the power-law exponent α calculated from a least-square fit

Here the power-law exponent α estimated by Clauset et al. (2009) and Virkar and Clauset (2014) (collectively call as VC14 α) is compared with α estimated from a least-square fit (LSF α). The purpose of the comparison is to provide an insight on how LSF α, which has been commonly used in previous studies, is comparable to α of Virkar and Clauset (2014). As mentioned in Introduction, the LSF method relies on a subjective judgment on the region of the straight line, bounded by the lower and upper limits of d. More importantly, the errors associated with LSF

α (whether from CFND or FND) are difficult to validate and are not properly normalized (see Clauset et al., 2009; Virkar and Clauset, 2014). For these reasons, VC14 α is used in our study; however, it is still of interest to see how LSF α compares to VC14 α.

For this purpose, LSF α is calculated by fitting the straight line on the log-log plot of CFND. An outlier-resistant least-square fit is used to minimize the flatting effects that normally occur toward the lower limit of d (smaller floes). The two sets of the floe size region are selected (200 m ≤ d ≤ 3000 m or 200 m ≤ d ≤ 1000 m), which define the lower and upper limits in the LSF. Note that the lower limit of LSF (d = 200 m) is smaller than the lowest x_{min} (d = 245 m) (estimated by Clauset et al., 2009; Virkar and Clauset, 2014). The upper limit of LSF (d = 1000 m or d = 3000 m) is selected based on the behavior of the straight line on the log-log plot. For most of the cases the upper limit of d = 3000 m is used, especially in July. The upper limit of d = 1000 m is used only for the cases in which small floes suddenly increase during mid-August breakup.

In overall, the mean difference in between VC14 α and LSF α is 0.11 ± 0.10, which is comparable to the mean error for VC14 α of 0.1. The maximum difference of 0.55 occurs on August 21 at C3. Note that the difference is higher than 0.1 for 43% of the data, and VC14 α is higher than LSF α for about 90% of those cases. These differences indicate that the lower limit of LSF may be too small, so that some of the data in the lower end still influence the fitting despite the use of the outlier-resistant fit. When a higher lower limit of LSF (d = 450 m) is used, the differences significantly reduce for some of those cases. However, the mean difference of all data remains almost the same; i.e., 0.12 ± 0.19. The maximum difference of 1.33 occurs on August 23 at C1.

Appendix C: Note on sea ice floe properties

In the pioneering work by Rothrock and Thorndike (1984), they found that the floe properties of area, mean caliper diameter, perimeter, and inscribed circle diameter were highly correlated, suggesting that a measurement of any one property can give an approximate value of any other. Since then, a number of studies reported floe properties as summarized in **Table C1**. These floe parameters from previous studies were calculated from aerial photographs or optical satellite imagery. In **Table C1**, the statistics of floe properties from TS-X data are compared with those from previous studies. The purpose of this comparison is two-fold. 1) The comparison provides indirect confirmation for consistency of FSD statistics from TS-X data, in comparison with aerial photographs and optical satellite data. Satellite SAR imagery used in this study typically contains much more noise, and floe boundary can be less well defined than aerial photographs or optical satellite data. 2) The comparison provides some insight on spatial and temporal variability of floe properties (if any).

In general, our statistics are consistent with the values from previous studies (**Table C1**). Regarding ratio A/d^2, our value was very comparable with Rothrock and Thorndike (1984) within the standard deviation. Our value for ratio P/d is most comparable with that of Toyota et al. (2006), but slightly higher

than that of Rothrock and Thorndike (1984). Ratios A/P^2 and d_{max}/d_{min} define the roundness of floes. They indicate more disc-like floes for the Rothrock and Thorndike (1984) and Hudson (1987) cases, but more elongated ellipse-like floes (=1.78) for the Toyota et al. (2006) case and also for our case. Interesting to note is that Hudson (1987) data were acquired in Canadian Arctic Archipelago, which contained large number of MYI floes. Rothrock and Thorndike (1984) data were acquired in the Beaufort Sea in August, 1978, which also potentially contained a large number of MYI floes. Toyota et al. (2006) data, by contrast, were acquired in the Sea of Okhotsk, an area of exclusively FYI floes. Our values lie between those of Rothrock and Thorndike (1984)/Hudson (1987) and Toyota et al. (2006). This finding suggests that MYI floes tend to have a more disc-like shape, whilst FYI floes tend to have a more elongated ellipse-like shape.

Our data also show that floe properties are highly correlated (R = 0.95–0.99; **Table C1**), similar to what was reported in previous studies. Regarding spatial and temporal variability, very little variation in floe properties was found between the clusters and over time, except a few cases that show very high ratios for d_{max}/d_{min} (up to 1.86) in late August. These cases, which contain more elongated ellipse-like floes, occur mainly due to ice banding which causes small floes to huddle together in elongated bands (Wadhams, 1983). In TS-X images, these ice bands, being tightly clustered together, are not separable and thus are sometimes seen as a single floe.

Appendix D: Relationship between α and mean floe size D

Here the relationship between the power-law exponent α and mean floe size D (a mean of mean caliper diameter d for each case) is considered. An empirical relationship of this type has been suggested in previous work by Perovich and Jones (2014) and Birnbaum and Lupkes (2002). In theory, a power-law FND ($n(d) - cd^{-\alpha}$) has a well-defined mean, if $\alpha > 1$ and $d \geq 1$; i.e., $D_{cal}(\alpha) = c\alpha/(\alpha - 1)$, where the normalization constant $c = x_{min}$ (estimated from Virkar and Causet, 2014). An empirical relationship drawn between α and D is shown with a hyperbola fit summarized in a hyperbola (see **Figure D1a**), $D_{reg}(\alpha) = c1\alpha/(\alpha - c2)$, where $c1 = 117.23$ and $c2 = 2.11$.

D_{cal} (black cross) and D_{reg} (green open circles) are compared against D (**Figure D1b**). As can be seen, D_{cal} largely overestimates D. The mean difference between D and D_{cal} is 368 m. This difference is significantly large, compared to the mean difference between D and D_{reg} (i.e., 72 m). The large errors in D_{cal} occur mainly because the selection of x_{min} is very sensitive to D_{cal}. For example, the largest difference between D and D_{cal} (Δ = 865 m) occurs on July 19 at C1, in which x_{min} is estimated to be 983 m from the data. On the other hand, the smallest difference between D and D_{cal} (Δ = 62 m) occurs on July 12 at C3, in which x_{min} is estimated to be 480 m. If x_{min} = 400 m is used for the July 19 case (the largest difference), then the difference quickly reduced to 12 m.

Assuming x_{min} linearly decreases with time, then x_{min} can be estimated as follows: $x_{min} = x_{min}(0) + a(JD - JD_0)$, where JD is Julian Day, JD_0 is the first JD, $x_{min}(0)$ is the initial x_{min}

at the first JD, and a is the slope (the degree of time variant). D_{cal} is then re-calculated with $x_{min}(0) = 450$ m and $a = 6$ (the results shown in red dots in **Figure D1b**). As can be seen, the difference between D_{cal} and D is greatly reduced. The mean difference between D_{cal} and D is now 53 m,

which is smaller than what was estimated between D and D_{reg}. The results suggest that the relationship between α and D is valid, if x_{min} can be estimated accurately. However, it is often difficult to estimate accurate x_{min} from the data, even with a good statistical method.

Appendix E: Tables and Figures

Table C1: Statistics on certain ratios of floe properties. In the table, A, P, d, d_{max} and d_{min} is floe area, perimeter, mean caliper diameter, maximum and minimum caliper diameters, respectively. R is the correlation coefficient. DOI: https://doi.org/10.1525/elementa.232.c1

A^a/d^2	P^b/d^c	A/P^2	$d_{max}{}^d/d_{min}{}^e$	Data source
$\pi/4 = 0.785$	$\pi = 3.14$	$(4\pi)^{-1} = 0.080$	1	Disc
1	4	0.0625	1	Square[f]
0.66 ± 0.05	3.17 ± 0.04	0.080 ± 0.065	1[g]	Rothrock and Thorndike, 1984, Aerial photographs, August, 1978, Beaufort Sea
–	$3.60^* \pm 0.002$	–	1.78 ± 0.4	Toyota et al., 2006, Landsat and aerial photographs, Feb 2003, Sea of Okhotsk
–	4.05[h]			Toyota and Enomoto, 2002, ADEOS/AVNIR, Feb 1997, Sea of Okhotsk
–	–	–	$1.5 – 1.6$	Hudson, 1987, Aerial photographs, April, 1982, Canadian Arctic Archipelago
0.61 ± 0.10 R = 0.98	3.57 ± 0.27 R = 0.99	0.049 ± 0.012 R = 0.95	1.64 ± 0.48 R = 0.96	This study, TerraSAR-X StripMap, July–August, 2014, Beaufort Sea

[a] floe area.
[b] floe perimeter.
[c] mean floe caliper diameter.
[d] maximum floe caliper diameter.
[e] minimum floe caliper diameter.
[f] d = a side of the square .
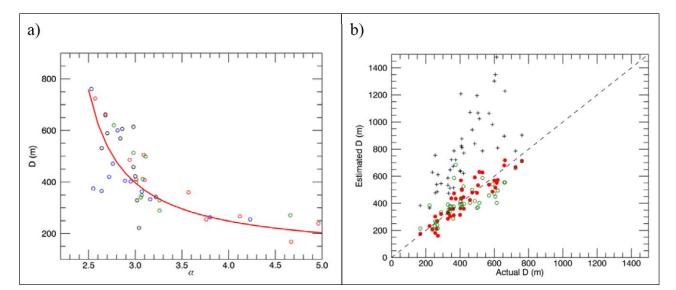[g] estimated from A/P^2.
[h] used circle diameter instead.

Figure D1: Relationship between power-law exponent α and mean floe size D. (a) A empirical relationship between power-law exponent α and mean floe size D. Black circles are the data points from Cluster 1, blue from Cluster 2, red from Cluster 3 and green from Cluster 4. The relationship can be summarized in a rectangular hyperbola, $D_{reg} = c1\alpha/(\alpha + c2)$, R^2 = 0.69, $c1 = 117.23$ and $c2 = -2.11$. **(b)** Comparison between D_{cal} (black cross) and D_{reg} (red open circle) against actual D (see the text for the definition). In (b), the red dots are the values calculated with a linearly varying x_{min}. DOI: https://doi.org/10.1525/elementa.232.d1

Data Accessibility Statement

Supplemental Files

The supplemental files for this article can be found as follows:

- **Table S1.** List of TS-X SM images used in this study. DOI: https://doi.org/10.1525/elementa.232.s1
- **Figure S1.** TS-X SM images showing the transition of an ice floe. DOI: https://doi.org/10.1525/elementa.232.s2
- **Video S1.** A sequence of sea ice extent maps overlaid with the locations of the clusters and the nearest ice edge for the period of June 1 to September 2, 2014. The sea ice extent maps are produced from MASIE-NH data (see text). The date is shown on the top of the map (e.g., yyyymmdd), and four numbers below the date are the distance to the nearest ice edge from C1 (1st left), C2 (2nd left), C3 (3rd left) and C4 (4th left). The GPS trajectory of C1, C2, C3 and C4 is shown in black, blue, red and purple colored line, respectively. The cluster locations on that date are shown in square symbols, and the corresponding ice edge location in plus symbols. The yellow colored region represents the open water area connected to the detected ice edge. DOI: https://doi.org/10.1525/elementa.232.s3

Competing interests

The authors have no competing interests to declare.

Author contributions

- Contributed to conception and design: BH, JW, TM, JR
- Contributed to acquisition of data: BH, HG, JW, TM, DP, AA
- Contributed to analysis and interpretation of data: BH, AS, CH, DP, AA
- Drafted and/or revised the article: ALL
- Approved the submitted version for publication: ALL

References

Arntsen, AE, Song, AJ, Perovich, DK and **Richter-Menge, JA** 2015 Observations of the summer breakup of an Arctic sea ice cover. *Geophys Res Lett* **42**. DOI: https://doi.org/10.1002/2015GL065224

Bingham, NH, Goldie, CM and **Teugels, JL** 1989 Regular variation. Cambridge University Press.

Birnbaum, G and **Lüpkes, C** 2002 A new parameterization of surface drag in the marginal sea ice zone. *Tellus A* **54**(1): 107–23. DOI: https://doi.org/10.1034/j.1600-0870.2002.00243.x

Clauset, A, Shalizi, CR and **Newman, MEJ** 2009 Power-law distributions in empirical data. *SIAM Review* **51**(4): 661–703. DOI: https://doi.org/10.1137/070710111

Cole, ST, Toole, JM, Lele, R, Timmermans, ML, Gallaher, SG, Stanton, TP, Shaw, W, Hwang, B, Maksym, T, Wilkinson, JP, Ortiz, M, Graber, HC, Rainville, L, Petty, AA, Farrell, S, Richter-Menge, J and **Haas, C** 2017 Ice and ocean velocity in the Arctic marginal ice zone: Ice roughness and momentum transfer. *Elem Sci Anth.* Under review for Marginal Ice Zone Processes in the Summertime Arctic Special Feature.

Cox, GFN and **Weeks, WF** 1983 Equations for determining the gas and brine volumes in sea ice samples. *Journal of Glaciology* **29**: 306–316. DOI: https://doi.org/10.1017/S0022143000008364

Doble, M, Wilkinson, J, Thomson, J, Rainville, L, Ortiz, M, Graber, HC, Hwang, B, Maksym, E, Bidlot, JR and **Wadhams, P** 2017 Directional wave measurements in the remnant sea ice of the summer Beaufort Sea. *Elem Sci Anth.* In press for Marginal Ice Zone Processes in the Summertime Arctic Special Feature.

Duke, T 2012 Introduction to the Global Fiducials Program. *AGU Fall Meeting, San Francisco,* 3–7 December.

Dumnont, D, Kohout, A and **Bertino, L** 2011 A wave-based model for the marginal ice zone including a floe breaking parameterization. *J Geophys Res* **116**(C04): 001. DOI: https://doi.org/10.1029/2010JC006682

European Centre for Medium-Range Weather Forecasts 2014 ECMWF ERA-Interim: reduced N256 Gaussian gridded surface level analysis time parameter data (ggas). *NCAS British Atmospheric Data Centre, 2017.* http://catalogue.ceda.ac.uk/uuid/3075228bcb09e90bf3717f9eeb0fed5b.

Gallaher, SG, Stanton, TP, Shaw, WJ, Cole, ST, Toole, JM, Wilkinson, JP, Maksym, E and **Hwang, B** 2016 Evolution of a Canada Basin ice-ocean boundary layer and mixed layer across a developing thermodynamically forced marginal ice zone, *J Geophys Res Oceans* **121**. DOI: https://doi.org/10.1002/2016JC011778

Holt, B and **Martin, S** 2001 The effect of a storm on the 1992 summer sea ice cover of the Beaufort, Chukchi, and East Siberian Seas. *J Geophys Res* **106**(C1): 1017–1032. DOI: https://doi.org/10.1029/1999JC000110

Horvat, C and **Tziperman, E** 2015 A prognostic model of the sea ice floe size and thickness distribution. *The*

Cryosphere Discuss **9**: 2955–2997. DOI: https://doi.org/10.5194/tcd-9-2955-2015

Horvat, C and **Tziperman, E** 2017 The evolution of scaling laws in the sea ice floe size distribution, *J Geophys Res* (in press).

Horvat, C, Tziperman, E and **Campin, J-M** 2016 Interaction of sea ice floe size, ocean eddies, and sea ice melting, *Geophys Res Lett* **43**: 8038–8090. DOI: https://doi.org/10.1002/2016GL069742

Hudson, RD 1987 Multiyear sea ice floe distribution in the Canadian Arctic Ocean. *J Geophys Res* **92**(C13): 14663–14669. DOI: https://doi.org/10.1029/JC092iC13p14663

Hwang, B, Elosegui, P and **Wilkinson, J** 2015 Small-scale deformation of an Arctic sea ice floe detected by GPS and satellite imagery. *Deep-Sea Res II.* DOI: https://doi.org/10.1016/j.dsr2.2015.01.007

Hwang, B, Ren, J, McCormack, S, Berry, C, Ben Ayed, I, Graber, HC and **Aptoula, E** 2017 A practical algorithm for the retrieval of the sea ice floe size distribution from high-resolution synthetic aperture radar imagery. *Elem Sci Anth.* Under review for Marginal Ice Zone Processes in the Summertime Arctic Special Feature.

Kwok, R and **Cunningham, GF** 2012 Deformation of the Arctic Ocean ice cover after the 2007 record minimum in summer ice extent. *Cold Reg Technol* **76−77**: 17–23. DOI: https://doi.org/10.1016/j.coldregions.2011.04.003

Kwok, R and **Untersteiner, N** 2011 New High-Resolution Images of Summer Arctic Sea Ice. *Eos* **92**(7): 53–54. DOI: https://doi.org/10.1029/2011EO070002

Langhorne, PJ, Squire, VA, Fox, C and **Haskell, TG** 1998 Break-up of sea ice by ocean waves, *Cold Reg Sci Technol* **27**: 438–442.

Lee, CM, Cole, S, Doble, M, Freitag, L, Hwang, P, Jayne, S, et al. 2012 Marginal Ice Zone (MIZ) Program: Science and Experiment Plan. *Technical Report APL-UW 1201.* Applied Physics Laboratory, University of Washington, Seattle, September 2012, 48.

National Ice Center and **National Snow and Ice Data Center** 2017 Compiled by Fetterer, F, Savoie, M, Helfrich, S and Clemente-Colón, P 2010 updated daily. Multisensor Analyzed Sea Ice Extent – Northern Hemisphere (MASIE-NH), Version 1. Northern Hemisphere (4 km). Boulder, Colorado USA. NSIDC: National Snow and Ice Data Center. May 09. DOI: https://doi.org/10.7265/N5GT5K3K

Onstott, RG 1992 SAR and scatterometer signature of sea ice, In: Carsey, F (ed.), *Microwave Remote Sensing of Sea Ice, Geophys Monogr Ser* **68**: 73–104, AGU, Washington, DC. DOI: https://doi.org/10.1029/gm068p0073

Perovich, DK and **Jones, KF** 2014 The seasonal evolution of sea ice floe size distribution. *J Geophys Res Oceans* **119**: 8767–8777. DOI: https://doi.org/10.1002/2014JC010136

Perovich, DK, Richter-Menge, JA and **Jones, KF** 2008 Sunlight, water, and ice: Extreme Arctic sea ice melt during the summer of 2007. *Geophys Res Lett* **35**(L11): 501. DOI: https://doi.org/10.1029/2008GL034007

Perovich, DK, Richter-Menge, JA and **Tucker, WB, III** 2001 Seasonal changes in sea ice morphology, *Annals of Glaciology* **33**: 171–176. DOI: https://doi.org/10.3189/172756401781818716

Polashenski, C, Perovich, DK, Richter-Menge, JA and **Elder, B** 2011 Autonomous observations of sea ice mass balance in seasonal ice. *Ann Glaciol* **52**: 18–26. DOI: https://doi.org/10.3189/172756411795931516

Rampal, P, Weiss, J and **Marsan, DJ** 2009 Positive trend in the mean speed and deformation rate of Arctic sea ice, 1979–2007. *J Geophys Res* **114**(C05): 013. DOI: https://doi.org/10.1029/2008JC005066

Roach, LA, Bitz, CM, Dean, SM and **Horvat, C** 2017 Impact of floe-size dependent processes on sea ice evolution. *paper presented at 14th Conference on Polar Meteorology and Oceanography,* Seattle, Washington, USA.

Rothrock, DA and **Thorndike, AS** 1984 Measuring the sea ice floe size distribution. *J Geophys Res* **89**: 6477–6486. DOI: https://doi.org/10.1029/JC089iC04p06477

Spreen, G, Kaleschke, L and **Heygster, G** 2008 Sea ice remote sensing using AMSR-E 89 GHz channels. *J Geophys Res* **113**(C02): S03. DOI: https://doi.org/10.1029/2005JC003384

Steele, M 1992 Sea ice melting and floe geometry in a simple ice-ocean model. *J Geophys Res* **97**: 17729–17738. DOI: https://doi.org/10.1029/92JC01755

Steer, A, Worby, A and **Heil, P** 2008 Observed changes in sea-ice floe size distribution during early summer in the western Weddell Sea. *Deep-Sea Research II* **55**: 933–942. DOI: https://doi.org/10.1016/j.dsr2.2007.12.016

Stern, HL, Schweiger, AJ, Stark, M, Zhang, J, Steele, M and **Hwang, B** 2017b Seasonal Evolution of the Sea-Ice Floe Size Distribution in the Beaufort and Chukchi Seas. *Elem Sci Anth.* Under review for Marginal Ice Zone Processes in the Summertime Arctic Special Feature.

Stern, HL, Schweiger, AJ, Zhang, J and **Steele, M** 2017a Is it possible to reconcile disparate studies of the sea-ice floe size distribution? *Elem Sci Anth.* Under review for Marginal Ice Zone Processes in the Summertime Arctic Special Feature.

Stroeve, JC, Markus, T, Boisvert, L, Miller, J and **Barrett, A** 2014 Changes in Arctic melt season and implications for sea ice loss. *Geophys Res Lett* **41**(4): 1216–1225. DOI: https://doi.org/10.1002/2013GL058951

Toyota, T and **Enomoto, H** 2002 Analysis of sea ice floes in the Sea of Okhotsk using ADEOS/AVNIR images. *paper presented at 16th International Symposium on Ice, Int. Assoc. for Hydraul Res.* Dunedin, New Zealand.

Toyota, T, Haas, C and **Tamura, T** 2011 Size distribution and shape properties of relatively small sea-ice floes in the Antarctic marginal ice zone in late winter.

Deep Sea Res II **58**: 1182–1193. DOI: https://doi.org/10.1016/j.dsr2.2010.10.034

Toyota, T, Takatsuji, S and **Nakayama, M** 2006 Characteristics of sea ice floe size distribution in the seasonal ice zone. *Geophys Res Lett* **33**(2): L02616. DOI: https://doi.org/10.1029/2005GL024556

Virkar, Y and **Clauset, A** 2014 Power-law distributions in binned empirical data. *The Annals of Applied Statistics* **8**(1): 89–119. DOI: https://doi.org/10.1214/13-AOAS710

Wadhams, P 1983 A mechanism for the formation of ice edge bands. *J Geophys Res* **88**(C5): 2813–2818. DOI: https://doi.org/10.1029/JC088iC05p02813

Wang, Y, Holt, B, Rogers, WE, Thomson, J and **Shen, HH** 2016 Wind and wave influences on sea ice floe size and leads in the Beaufort and Chukchi Seas during the summer-fall transition 2014, *J Geophys Res Oceans* **121**: 1502–1525. DOI: https://doi.org/10.1002/2015JC011349

Weeks, WF 1998 Growth conditions and structure and properties of sea ice, In: Leppäranta, M. (ed.), *Physics of Ice-Covered Seas* **1**: 25–104. Helsinki University Press, Helsinki.

Williams, TD, Bennetts, L, Squire, VA, Dumont, D and **Bertino, L** 2013a Wave-ice interactions in the marginal ice zone. Part 1: Theoretical foundations. *Ocean Model* **71**: 81–91. DOI: https://doi.org/10.1016/j.ocemod.2013.05.010

Williams, TD, Bennetts, L, Squire, VA, Dumont, D and **Bertino, L** 2013b Wave-ice interactions in the marginal ice zone. Part 2: Numerical implementation and sensitivity studies along 1D transects of the ocean surface. *Ocean Model* **71**: 92–101. DOI: https://doi.org/10.1016/j.ocemod.2013.05.011

Williams, TD, Rampal, P and **Bouillon, S** 2017 Wave-ice interactions in the neXtSIM sea-ice model. *The Cryosphere Discuss.* DOI: https://doi.org/10.5194/tc-2017-24

Zhang, J, Lindsay, R, Schweiger, A and **Rigor, I** 2012 Recent changes in the dynamic properties of declining Arctic sea ice: a model study. *Geophys Res Lett* **39**(L2): 0503. DOI: https://doi.org/10.1029/2012GL053545

Zhang, J, Schweiger, A, Steele, M and **Stern, H** 2015 Sea ice floe size distribution in the marginal ice zone: Theory and numerical experiments, *J. Geophys Res* **120**. DOI: https://doi.org/10.1002/2015JC010770

Zhang, J, Stern, H, Hwang, B, Schweiger, A, Steele, M and **Stark, M** 2016 Modeling the seasonal evolution of the Arctic sea ice floe size distribution. *Elem Sci Anth.* **4**: 000126. DOI: https://doi.org/10.12952/journal.elementa.000126